WARWICK
THE UNIVERSITY OF WARWICK

Original citation:
Liu, Teng, Gao, Weiguo, Zhang, Dawei, Zhang, Yifan, Chang, Wenfen, Liang, Cunman and Tian, Yanling. (2017) Analytical modeling for thermal errors of motorized spindle unit. International Journal of Machine Tools and Manufacture, 112 . pp. 53-70.

Permanent WRAP URL:
http://wrap.warwick.ac.uk/94027

Copyright and reuse:
The Warwick Research Archive Portal (WRAP) makes this work by researchers of the University of Warwick available open access under the following conditions. Copyright © and all moral rights to the version of the paper presented here belong to the individual author(s) and/or other copyright owners. To the extent reasonable and practicable the material made available in WRAP has been checked for eligibility before being made available.

Copies of full items can be used for personal research or study, educational, or not-for-profit purposes without prior permission or charge. Provided that the authors, title and full bibliographic details are credited, a hyperlink and/or URL is given for the original metadata page and the content is not changed in any way.

Publisher's statement:
© 2017, Elsevier. Licensed under the Creative Commons Attribution-NonCommercial-NoDerivatives 4.0 International http://creativecommons.org/licenses/by-nc-nd/4.0/

A note on versions:
The version presented here may differ from the published version or, version of record, if you wish to cite this item you are advised to consult the publisher's version. Please see the 'permanent WRAP URL' above for details on accessing the published version and note that access may require a subscription.

For more information, please contact the WRAP Team at: wrap@warwick.ac.uk

warwick.ac.uk/lib-publications

*Manuscript without author identifiers
Click here to view linked References

Analytical Modeling for Thermal Errors of Motorized Spindle Unit

Abstract: Modeling method investigation about spindle thermal errors is significant for spindle thermal optimization in design phase. To accurately analyze the thermal errors of motorized spindle unit, this paper assumes approximately that 1) spindle linear thermal error on axial direction is ascribed to shaft thermal elongation for its heat transfer from bearings, and 2) spindle linear thermal errors on radial directions and angular thermal errors are attributed to thermal variations of bearing relative ring displacements. Based on prerequisites, an analytical modeling method is developed to analyze these spindle thermal errors. Firstly, thermal-mechanical models of rotating ring geometry and interference assembled rotating ring geometries are established, for thermal variation modeling of relative ring displacements of short cylindrical roller bearing and angular contact ball bearing. Secondly, these thermal variation models are associated with heat-fluid-solid coupling FE (finite element) simulation technique, to model spindle linear thermal errors on radial /axial directions and angular thermal errors by the analytical simulation method. Consequently, verification experiments clarify that the presented method is accurate for spindle thermal errors modeling, and can be effectively applied into the design and development phases of motorized spindle units.

Keywords: Motorized spindle unit, Thermal error, Thermal variation of bearing relative ring displacement, Short cylindrical roller bearing, Angular contact ball bearing, FE (finite element)

Nomenclature

$\varepsilon_r/\varepsilon_\varphi$	Internal radial / circumferential strain of rotating ring geometry
$u/\ r$	Internal radial displacement / distance of rotating ring geometry (m)
σ_r/σ_φ	Internal radial / circumferential stress of rotating ring geometry (Pa)
ω	Angular velocity (rad/s)
$\rho\ /\ \rho^{-1(2)}$	Density of single rotating ring geometry / 1(2) in rotating ring geometries (Kg/m^3)
$E\ /\ E^{-1(2)}$	Elastic modulus of single rotating ring geometry / 1(2) in rotating ring geometries (Pa)
$\mu\ /\ \mu^{-1(2)}$	Poisson's ratio of single rotating ring geometry / 1(2) in rotating ring geometries
$\alpha^{S}\ /\ \alpha^{-1(2)}$	Thermal expansion coefficient of single rotating ring geometry / 1(2) in rotating ring geometries (℃$^{-1}$)
t	Moment (s)
T_0	Initial temperature (℃)
$T\ /\ T_C\ /\ T_A$	Temperature of rotating ring geometry / short cylindrical roller bearing / angular contact ball bearing (℃)
$D_1/\ D_2$	Inner / outer diameter of rotating ring geometry (m)
$P/\ P_{1(2)}$	Compressive stress of rotating ring geometries / onto inner (outer) cylindrical surface of single rotating ring geometry (Pa)
$u^{\mathrm{II}\_1(2)\_\mathrm{na}}\ /\ u^{\mathrm{II}\_1(2)}$	Displacements of outer edge of ring geometry 1 (the inner edge of ring geometry 2) caused by the rotating ring geometries temperature rise exclusively / mutual compressive stress exclusively (m)
$I\ /\ I_{\mathrm{CO(I)}}\ /\ I_{\mathrm{AO(I)}}$	Interference fit value of rotating ring geometries / short cylindrical roller bearing / angular contact ball bearing-bearing housing (spindle shaft) (m)
$D^{\mathrm{I}}\ /\ D^{\mathrm{II}}/\ D^{\mathrm{III}}$	Diameter Ⅰ/ Ⅱ/ Ⅲ of rotating ring geometries (m)
$u^{\mathrm{I}}\ /\ u^{\mathrm{III}}$	Displacements of diameter Ⅰ / Ⅲ of rotating ring geometries caused

	by both their temperature rise and mutual compressive stress (m)
Z	Number of bearing rollers
Ψ_j / $\Delta\Psi$	Roller angular position / interval of spindle bearing (rad)
$\rho_{\mathrm{C}}^{\mathrm{bea}}$ / $\rho_{\mathrm{A}}^{\mathrm{bea}}$	Density of short cylindrical roller bearing / angular contact ball bearing (Kg/m^3)
E^{spi} / $E_{\mathrm{C}}^{\mathrm{bea(hou)}}$ / $E_{\mathrm{A}}^{\mathrm{bea(hou)}}$	Elastic modulus of spindle shaft / short cylindrical roller bearing (its bearing housing) / angular contact ball bearing (its bearing housing) (Pa)
μ^{spi} / $\mu_{\mathrm{C}}^{\mathrm{bea(hou)}}$ / $\mu_{\mathrm{A}}^{\mathrm{bea(hou)}}$	Poisson's ratio of spindle shaft / short cylindrical roller bearing (its bearing housing) / angular contact ball bearing (its bearing housing)
α^{spi} / $\alpha_{\mathrm{C}}^{\mathrm{bea(hou)}}$ / $\alpha_{\mathrm{A}}^{\mathrm{bea(hou)}}$	Thermal expansion coefficient of spindle shaft / short cylindrical roller bearing (its bearing housing) / angular contact ball bearing (its bearing housing) (℃$^{-1}$)
$P_{\mathrm{CO(I)}}$ / $P_{\mathrm{AO(I)}}$	Compressive stress of outer (inner) ring of short cylindrical roller bearing / angular contact ball bearing (Pa)
l/d_{C} (Δl / Δd_{C})	Roller axial / radial length (thermal deformation) of short cylindrical roller bearing (m)
$D^{\mathrm{I}}{}_{\mathrm{CO}}$/ $D^{\mathrm{II}}{}_{\mathrm{CO}}$/ $D^{\mathrm{III}}{}_{\mathrm{CO}}$	Outer diameter Ⅰ/ Ⅱ/ Ⅲ of short cylindrical roller bearing (m)
$D^{\mathrm{I}}{}_{\mathrm{CI}}$/ $D^{\mathrm{II}}{}_{\mathrm{CI}}$/ $D^{\mathrm{III}}{}_{\mathrm{CI}}$	Inner diameter Ⅰ/ Ⅱ/ Ⅲ of short cylindrical roller bearing (m)
$u_{\mathrm{CO}}^{\mathrm{I}}$ / $u_{\mathrm{CI}}^{\mathrm{III}}$	Displacement of outer/ inner groove of short cylindrical roller bearing (m)
d_{A} / Δd_{A}	Roller diameter length / diameter thermal deformation of angular contact ball bearing (m)
$l_{\mathrm{i(o)}}$ / $\Delta l_{\mathrm{i(o)}}$	Length / length thermal deformation of inner (outer) grooves of angular contact ball bearing (m)
$D^{\mathrm{I}\_i}{}_{\mathrm{AO}}$, i=1/ 2/ 3	Outer diameter Ⅰ_1/ 2/ 3 of angular contact ball bearing (m)
$D^{\mathrm{II}}{}_{\mathrm{AO}}$/ $D^{\mathrm{III}}{}_{\mathrm{AO}}$	Outer diameter Ⅱ/ Ⅲ of angular contact ball bearing (m)
$D^{\mathrm{I}}{}_{\mathrm{AI}}$/ $D^{\mathrm{II}}{}_{\mathrm{AI}}$	Inner diameter Ⅰ/ Ⅱ of angular contact ball bearing (m)
$D^{\mathrm{III}\_i}{}_{\mathrm{AI}}$, i = 1'/ 2'/ 3'	Inner diameter Ⅲ_1'/ 2'/ 3' of angular contact ball bearing (m)

$u_{\mathrm{AO}}^{\mathrm{I}\_i}, i=1/2/3$	Displacement of inner edge $1/2/3$ of outer ring of angular contact ball bearing (m)
$u_{\mathrm{AI}}^{\mathrm{III}\_i}, i=1'/2'/3'$	Displacement of outer edge $1'/2'/3'$ of inner ring of angular contact ball bearing (m)
$Q_{\mathrm{Co(i)}j}$ / $Q_{\mathrm{Ao(i)}j}$	Contact stress between *j*th roller and outer (inner) groove of short cylindrical roller bearing/ angular contact ball bearing (Pa)
$\delta_{\mathrm{Co(i)}j}$ / $\delta_{\mathrm{Ao(i)}j}$	Radial displacements of outer (inner) groove locations contacted with *j*th roller of short cylindrical roller bearing/ angular contact ball bearing (m)
$F_{\mathrm{C(A)}j}^{\mathrm{cen}}$	Centrifugal force of *j*th roller of short cylindrical roller bearing (angular contact ball bearing) (N)
$K_{\mathrm{C}} / K_{\mathrm{Ao(i)}j}$	Contact stiffness between roller and outer (inner) groove of short cylindrical roller bearing / angular contact ball bearing (Pa)
$P_{\mathrm{dC(A)}}$	Diametric clearance of short cylindrical roller bearing/ angular contact ball bearing (m)
$d_{\mathrm{m\_C(A)}}$	Pitch diameter of short cylindrical roller bearing (angular contact ball bearing) (m)
$\delta_{\mathrm{C\_r}} / \overline{\delta_{\mathrm{C\_r}}}$	Relative ring displacement/ thermal variation of relative ring displacement of short cylindrical roller bearing (m)
$F_{\mathrm{C\_r}}$	Radial force of short cylindrical roller bearing (N)
n_{m}	Roller orbital speed of short cylindrical roller bearing (R/min)
$r_{\mathrm{i(o)}}$/ A	Radius/ curvature center distance of inner (outer) grooves of angular contact ball bearing (m)
$u_{\mathrm{ox(y)}}$	Curvature center thermal displacement of outer groove of angular contact ball bearing on X(Y) axis (m)
$\alpha / \alpha_{\mathrm{o(i)}j}$	Initial contact angle / *j*th roller-outer (inner) groove contact angle of angular contact ball bearing (Rad)
$F_{\mathrm{A\_r}} / F_{\mathrm{A\_a}}$	Radial/ axial force of angular contact ball bearing (N)

M_{A}	Bending moment of angular contact ball bearing (Nm)
$\delta_{\mathrm{A\_r}}/\overline{\delta_{\mathrm{A\_r}}}$ ($\delta_{\mathrm{A\_r(g)}}/\overline{\delta_{\mathrm{A\_r(g)}}}$)	Radial relative ring displacement/ thermal variation of radial relative ring displacement of angular contact ball bearing (front bearing group) (m)
$\delta_{\mathrm{A\_a}}/\overline{\delta_{\mathrm{A\_a}}}$ ($\delta_{\mathrm{A\_a(g)}}/\overline{\delta_{\mathrm{A\_a(g)}}}$)	Axial relative ring displacement/ thermal variation of axial relative ring displacement of angular contact ball bearing (front bearing group) (m)
$\theta/\overline{\theta_{\mathrm{A\_r}}}$ ($\theta_{\mathrm{A\_r(g)}}/\overline{\theta_{\mathrm{A\_r(g)}}}$)	Angular relative ring displacement/ thermal variation of angular relative ring displacement of angular contact ball bearing (front bearing group) (Rad)
δ^{*}	Bearing contact displacement with the dimension 1
M_{gj}	Gyroscopic moment of *j*th bearing roller (Nm)
$\omega_{\mathrm{R}}/\omega_{\mathrm{m}}$	Roller geostrophic /orbit velocity of angular contact ball bearing (Rad/s)
J	Roller rotary inertia of angular contact ball bearing (Kgm^2)
β	Roller yaw angle of angular contact ball bearing (Rad)
$\Re_{\mathrm{i}}$	Orbit radius of inner groove curvature center of angular contact ball bearing (m)
$Q_{\mathrm{Fr/Mo/Ba}}$	Heat power of spindle front bearings/ motor/ back bearing (W)
$Q_{\mathrm{Fr/Mo/Ba}}'$	Heat power of spindle front bearings/ motor/ back bearing after accurate correction (W)
n	Rotating speed of spindle (RPM)
M_0 / M_1	Bearing frictional torque for lubricant viscosity/applied force load (Nmm)
f_0 / f_1	Factor related to bearing type and lubrication method / applied force load
v_0	Kinematics viscosity of lubricant (mm^2/s)
F_{β}	Applied force load onto bearing (N)
D_{m}	Mean diameter of the bearing (mm)
$h_{\mathrm{f/n}}$	Coefficient of forced/ natural convection heat transfer (W/(m^2K))
Nu	Nusselt number
λ	Thermal conductivity of air (w/(m·K))

d_e / l_e	Diameter / length of the spindle part (m)
Re / Pr	Reynolds number / Prandtl number of air
u_{air}	Flow velocity of air (m/s)
v_{air}	Kinematics viscosity of air (m^2/s)
T_S / T_{am}	Coolant supply / ambient temperature (℃)
V_S	Coolant supply volume flow rate (L/min)
ρ_{oil_sol} /ρ_{oil}	Coolant oil or solid / solid density (Kg/m^3)
k_{oil_sol}	Thermal conductivity of coolant oil or solid (w/(m·K))
H_{en}	Energy content per unit mass (J)
p	Pressure (Pa)
$\vec{v}$ / $\overline{\overline{\tau}}$	Velocity vector/ Stress tensor
S_h	Heat energy generated by volumetric heat source (W)
u/ v/ w	Coolant flowing velocity on X/Y/Z direction (m/s)
$\nabla \bullet (\overline{\overline{\tau}}\, \vec{v})$	Energy caused by viscous power dissipation of flowing coolant (W)
$\nabla \bullet (k \nabla T)$	Heat transfer among solid, flowing coolant and ambient air (W)
$k(b)_{Q\_\mathrm{Fr/Mo/Ba}}$ / $k(b)_{h\_\mathrm{f/n}}$	Proportionality (deviation) correction coefficient for heat generation power/ heat transfer coefficient
$T_{\mathrm{Fr/Mo/Ba}}$ / $\overline{\overline{T}}_{\mathrm{Fr/Mo/Ba}}$	Spindle simulated / experimental temperature (℃)
G^{spi}	Gravity of spindle rotating unit (N)
$F_{X\backslash Y\backslash Z}$	Force component of cutting load on X\Y\Z axis (N)
$M_{X\backslash Y}$	Moment component of cutting load about X\Y\Z axis (Nm)
F_P	Axial preload for spindle front bearing group (N)
L_{1-2}/ L_{2-3}/ L_{3-4}	Distance of bearing 1 - 2/ 2 - 3/ 3 - 4 (m)
L / S / X_G	Distance of front bearing 4 - spindle nose / back bearing - front bearing 1 / back bearing - gravity center of spindle rotating unit (m)
$\overline{\delta_X}$ / $\overline{\delta_Y}$ / $\overline{\delta_Z}$	Linear thermal error of motorized spindle unit on X/Y/Z axis (μm)

$\overline{\varepsilon_{\mathrm{X}}} / \overline{\varepsilon_{\mathrm{Y}}}$	Angular thermal error of motorized spindle unit about X/Y axis (rad)
$\overline{\delta_{\mathrm{X(A)}}} / \overline{\delta_{\mathrm{Y(A)}}} / \overline{\delta_{\mathrm{X(B)}}} / \overline{\delta_{\mathrm{Y(B)}}}$	Detected values of eddy current displacement sensors X(A)/Y(A)/X(B)/Y(B) (μm)

1 Introduction

Being the key functional component of precision machine tool, the motorized spindle unit has a compact structure combining its built-in motor and spindle bearings. This structure makes the motorized spindle unit have advanced characteristics such as high speed, precision, and rigidity, and thus provide itself with a widespread manufacturing application in recent years. However, the structural characteristic of motorized spindle unit also gives rise to negative effects due to its internal thermal factors on machine comprehensive accuracy [1]. Generally, the internal heat generation and dissipation, mainly from the motor and bearings, of motorized spindle unit determines its structural temperature fluctuation in machining process, and then causes the spindle thermal elastic deformation resulting in the geometric and shape errors of machined workpieces. With growing promotion of precision machining level, thermal deformation of motorized spindle unit has an increasingly obvious disturbance onto machine accuracy and accuracy stability [2]. Therefore, it is essential to study the thermal characteristic mechanism of motorized spindle unit and establish the accurate analyzing and modeling method of spindle thermal error, and these investigations have crucial theoretical and engineering values for the design level improvement of motorized spindle units and the accuracy degeneration avoidance of precision machine tools.

Spindle thermal characteristic modeling is the critical basis for spindle thermal error analyses, and various latest research efforts were based on experimental modeling methods to establish the relationship between spindle thermal errors and its other thermal characteristics. Pahk [3] developed a spindle thermal error measuring system, and then used multiple linear regression, neural network and system identification methods respectively to establish spindle temperature - thermal error model. Ko [4] studied experimentally spindle thermal error characteristics in its operation start and stop phases, and found out the relationship between spindle temperature - thermal error measuring. Chen [5] presented an auto-regression dynamic thermal error model with the consideration of the spindle temperature history and speed information. Brecher [6] introduced an indirect spindle thermal error compensation approach, whose model inputs include spindle temperature, rotational speed and motor current values being related to spindle drive torque. Kang [7] adopted forward neural network and hybrid filter methods to predict spindle thermal errors based on its temperature testing, and thus enhanced prediction accuracy and calculation speed. Gomez-Acedo [8] presented an experimentally identified model based on a large gantry-type milling machine. The model inputs are spindle speed, temperatures of main motor gearbox and room air, and outputs are estimations of the thermal drift of the machine tool center point along the 3 axes in different positions within the working volume. In the study of Mayer [9], thermally induced volumetric distortion errors of a five-axis machine tool are modeled in relation to the machine activity sequence during which the power at each of the five axis motors and the spindle are measured. Liu [10] tested radial thermal drift error in Y-direction and temperatures in key points of the spindle of a vertical machining center using its different rotating speeds, for the establishment of radial thermal drift error models under different postures. These experimental modeling activities are of great value onto the recognition about spindle thermal characteristics. Nevertheless, they are lacking in mechanism discussions for spindle thermal errors occurrence, and then difficult to be used to predict and analyze thermal characteristics of motorized spindle unit, during its design and development phase.

Some other researching activities placed emphasis on the analytical and simulation modeling methods for the spindle thermal characteristics. Zhao [11] simulated the temperature and thermal error behaviors of a CNC machine tool spindle by FE method, in which the coolant heat transfer is considered approximately as a constant temperature load. Creighton [12] conducted the numerical simulation to get the temperature distribution and thermal growth of a high speed micro milling spindle, with its bearings supporting and motor being considered approximately as main heat sources. Holkup [13] and Li [14] considered the spindle circulating coolant heat transfer as the forced heat convection, and established the thermal-structure coupling simulation model of the high-speed precision spindle to predict and analyze the spindle transient temperature and thermal error characteristics. Jiang [15] used FEM method to analyze spindle temperature distribution, and the variable spindle preload was determined based on bearing temperature rise constraint at high speed range. At low speed range, the spindle preload was resolved by bearing fatigue life. The dynamic stiffness of the variable preload spindle was analyzed utilizing Transfer Matrix Method and a nonlinear bearing model including the centrifugal force and gyroscopic effects. Chen [16] used FEM to simulate the temperature and thermal error behaviors of a hydrostatic spindle unit, with the assumption that the forced convection heat transfer between hydrostatic oil film and the spindle structure is a constant load. Zheng [17] developed a thermal model for high speed press system based on the fractal model and the change of the heat generation power by FE method, to explore its temperature histories and the time for reaching its thermal equilibrium condition. Lee [18] investigated the association between spindle vibration characteristics and thermal errors by an accurate numerical thermal model of motorized spindle unit. Ma [19] established the theoretical model of spindle thermal resistance - bearing stiffness to improve the model accuracy of the spindle temperature and thermal error predictions. These studies tried to establish theoretical models to analyze and predict the thermal characteristics of motorized spindle unit. But in these models, there are insufficient influence considerations of bearing thermal characteristic variations on spindle errors, which reduced their prediction accuracy and value in some degrees.

With the emphasis that the spindle thermal errors are closely related to thermal variations of relative ring displacements of spindle bearings, this paper introduces a method to analyze accurately thermal errors of motorized spindle unit. This method is realized by the analytical modeling based on the heat-fluid-solid coupling FE simulation technology. The structure of this paper is arranged as follows: Section 2 introduces thermal-mechanical models of rotating ring geometry and interference assembled rotating ring geometries for theoretical preparations. Then the conclusions of Section 2 are applied into thermal variation calculations of relative ring displacements of short cylindrical roller bearing and angular contact ball bearing in Section 3. In Section 4, the obtained thermal variations of bearing relative ring displacements are utilized with the heat-fluid-solid coupling FE simulations for motorized spindle unit, so as to analyze spindle thermal errors. The reliability and accuracy of the developed analytical modeling method for spindle thermal errors is verified by experiments in Section 5. Finally, Section 6 gives the conclusions and prospects of this study.

2 Theoretical preparations for thermal modeling of spindle bearings

This section firstly discusses the thermo-mechanical modeling of a rotating ring geometry, and then its conclusions result in the establishment of a thermo-mechanical displacement model for interference assembled rotating ring geometries. These are necessary theoretical preparations for the thermal variation modeling of relative ring displacements of spindle bearings.

2.1 Thermo-mechanical modeling of rotating ring geometry

As depicted in Fig. 1, the presented rotating ring geometry has an angular velocity ω about the Z axis. Its material has the constant properties, and its inner and outer diameters are D_1 and D_2 respectively. Specially, its inner and outer cylindrical surfaces are with the stress P_1 and P_2 respectively. According to the theoretical method about ring geometry introduced in classical book [20], the radial displacement of any location of the rotating ring geometry caused by its thermo-mechanical effect can be solved by:

$$u=\alpha^{S}(1+\mu)\frac{1}{r}\int_{\frac{D_1}{2}}^{r}(T_t-T_0)\xi \mathrm{d}r+\frac{r(1-\mu)}{E\left(D_1^2-D_2^2\right)}\left[D_2^{\,2}P_2-D_1^{\,2}P_1-4\alpha^{S}E\int_{\frac{D_1}{2}}^{\frac{D_2}{2}}(T_t-T_0)\xi \mathrm{d}r-\frac{\rho\omega^2(3+\mu)}{32}\left(D_2^{\,4}-D_1^{\,4}\right)\right]$$
$$+\frac{D_1^{\,2}D_2^{\,2}(1+\mu)}{4rE\left(D_1^2-D_2^2\right)}\left[P_2-P_1-\frac{4\alpha^{S}E}{D_2^2}\int_{\frac{D_1}{2}}^{\frac{D_2}{2}}(T_t-T_0)\xi \mathrm{d}r-\frac{\rho\omega^2(3+\mu)}{32}\left(D_2^{\,2}-D_1^{\,2}\right)\right]-\frac{(1-\mu^2)\rho\omega^2 r^3}{8E} \quad (1)$$

This conclusion give rise to the thermo-mechanical modeling of interference assembled rotating ring geometries.

2.2 Thermo-mechanical modeling of interference assembled rotating ring geometries

As depicted in Fig. 2, ring geometries 1 and 2 have inner/ outer diameters $D^{\mathrm{I}}/D^{\mathrm{II}}$ and $D^{\mathrm{II}}/D^{\mathrm{III}}$ respectively. They are assembled by interference method and have the common angular velocity ω about Z axis. Because the time-varying structural temperature T_t of these rotating ring geometries can lead to their thermal deformations, their interference fit I_t and compressive stress P_t are influenced by their structural temperature rise T_t - T_0.

2.2.1 Structural temperature rise - interference compressive stress modeling of rotating ring geometries

If the rotating ring geometries in Fig. 2 is not assembled with interference (without the compressive stress), the outer edge of ring geometry 1 and the inner edge of ring geometry 2 will have the displacements caused by their structural temperature rise T_t - T_0 exclusively. These thermal displacements can be seen as the thermal variations of the interference fit scale, when the rotating ring geometries 1 and 2 are assembled together by interference method:

$$I_t-I_0=u_t^{\mathrm{II\_1\_na}}+u_t^{\mathrm{II\_2\_na}} \quad (2)$$

Meanwhile, the time-varying interference fit scale can be considered to be the displacement sum caused by the corresponding time-varying mutual compressive stress:

$$I_t = u_t^{\mathrm{II\_1}} + u_t^{\mathrm{II\_2}} \tag{3}$$

Equation (3) is substituted into equation (2) to get:

$$u_t^{\mathrm{II\_1}} + u_t^{\mathrm{II\_2}} = u_t^{\mathrm{II\_1\_na}} + u_t^{\mathrm{II\_2\_na}} + I_0 \tag{4}$$

According to equation (1), the outer edge thermal displacement of ring geometry 1 and the inner edge thermal displacement of ring geometry 2 can be obtained based on the non-assembly state (Ring edge displacements are caused by structural temperature rise T_t - T_0 exclusively) and the assembly state (Ring edge displacements are caused by compressive stress exclusively):

Non-assembly state:

$$\begin{cases} u_t^{\mathrm{II\_1\_na}} = 2\alpha^{-1}\left[\dfrac{\left(1+\mu^{-1}\right)}{D^{\mathrm{II}}} - \dfrac{D^{\mathrm{II}}\left(1-\mu^{-1}\right)}{\left(D^{\mathrm{I}}\right)^2-\left(D^{\mathrm{II}}\right)^2} - \dfrac{\left(D^{\mathrm{I}}\right)^2\left(1+\mu^{-1}\right)}{D^{\mathrm{II}}\left[\left(D^{\mathrm{I}}\right)^2-\left(D^{\mathrm{II}}\right)^2\right]}\right]\displaystyle\int_{\frac{D^{\mathrm{I}}}{2}}^{\frac{D^{\mathrm{II}}}{2}}\left(T_t-T_0\right)\xi\,\mathrm{d}r \\ +\dfrac{\rho^{-1}\omega^2 D^{\mathrm{II}}}{64E^{-1}}\left[\left(3+\mu^{-1}\right)\left(1-\mu^{-1}\right)\left(D^{\mathrm{II}}\right)^2+\left(3+\mu^{-1}\right)\left(1-\mu^{-1}\right)\left(D^{\mathrm{I}}\right)^2+\left(3+\mu^{-1}\right)\left(1+\mu^{-1}\right)\left(D^{\mathrm{I}}\right)^2-\left(D^{\mathrm{II}}\right)^2+\left(\mu^{-1}\right)^2\left(D^{\mathrm{II}}\right)^2\right] \\ u_t^{\mathrm{II\_2\_na}} = \dfrac{-4\alpha^{-2}D^{\mathrm{II}}}{\left(D^{\mathrm{II}}\right)^2-\left(D^{\mathrm{III}}\right)^2}\displaystyle\int_{\frac{D^{\mathrm{II}}}{2}}^{\frac{D^{\mathrm{III}}}{2}}\left(T_t-T_0\right)\xi\,\mathrm{d}r \\ +\dfrac{\rho^{-2}\omega^2 D^{\mathrm{II}}}{64E^{-2}}\left[\left(1-\mu^{-2}\right)\left(3+\mu^{-2}\right)\left(D^{\mathrm{III}}\right)^2+\left(1-\mu^{-2}\right)\left(3+\mu^{-2}\right)\left(D^{\mathrm{II}}\right)^2+\left(3+\mu^{-2}\right)\left(1+\mu^{-2}\right)\left(D^{\mathrm{III}}\right)^2-\left(D^{\mathrm{II}}\right)^2+\left(D^{\mathrm{II}}\right)^2\left(\mu^{-2}\right)^2\right] \end{cases} \tag{5}$$

Assembly state:

$$\begin{cases} u_t^{\mathrm{II\_1}} = \dfrac{D^{\mathrm{II}}\left[\left(D^{\mathrm{II}}\right)^2\left(1-\mu^{-1}\right)+\left(D^{\mathrm{I}}\right)^2\left(1+\mu^{-1}\right)\right]}{2E^{-1}\left[\left(D^{\mathrm{I}}\right)^2-\left(D^{\mathrm{II}}\right)^2\right]}\bullet P_t \\ +\dfrac{\rho^{-1}\omega^2 D^{\mathrm{II}}}{64E^{-1}}\left[\left(3+\mu^{-1}\right)\left(1-\mu^{-1}\right)\left(D^{\mathrm{II}}\right)^2+\left(3+\mu^{-1}\right)\left(1-\mu^{-1}\right)\left(D^{\mathrm{I}}\right)^2+\left(3+\mu^{-1}\right)\left(1+\mu^{-1}\right)\left(D^{\mathrm{I}}\right)^2-\left(D^{\mathrm{II}}\right)^2+\left(\mu^{-1}\right)^2\left(D^{\mathrm{II}}\right)^2\right] \\ u_t^{\mathrm{II\_2}} = -\dfrac{D^{\mathrm{II}}\left[\left(D^{\mathrm{II}}\right)^2\left(1-\mu^{-2}\right)+\left(D^{\mathrm{III}}\right)^2\left(1+\mu^{-2}\right)\right]}{2E^{-2}\left[\left(D^{\mathrm{II}}\right)^2-\left(D^{\mathrm{III}}\right)^2\right]}\bullet P_t \\ +\dfrac{\rho^{-2}\omega^2 D^{\mathrm{II}}}{64E^{-2}}\left[\left(1-\mu^{-2}\right)\left(3+\mu^{-2}\right)\left(D^{\mathrm{III}}\right)^2+\left(1-\mu^{-2}\right)\left(3+\mu^{-2}\right)\left(D^{\mathrm{II}}\right)^2+\left(3+\mu^{-2}\right)\left(1+\mu^{-2}\right)\left(D^{\mathrm{III}}\right)^2-\left(D^{\mathrm{II}}\right)^2+\left(D^{\mathrm{II}}\right)^2\left(\mu^{-2}\right)^2\right] \end{cases} \tag{6}$$

Equations (5) and (6) are substituted into equation (4) for the interference compressive stress modeling of rotating ring geometries:

$$P_t = \frac{I_0 + 2\alpha^{-1}\left[\frac{\left(1+\mu^{-1}\right)}{D^{\mathrm{II}}} - \frac{D^{\mathrm{II}}\left(1-\mu^{-1}\right)}{\left(D^{\mathrm{I}}\right)^2-\left(D^{\mathrm{II}}\right)^2} - \frac{\left(D^{\mathrm{I}}\right)^2\left(1+\mu^{-1}\right)}{D^{\mathrm{II}}\left[\left(D^{\mathrm{I}}\right)^2-\left(D^{\mathrm{II}}\right)^2\right]}\right]\int_{\frac{D^{\mathrm{I}}}{2}}^{\frac{D^{\mathrm{II}}}{2}}\left(T_t-T_0\right)\xi \mathrm{d}r - \frac{4\alpha^{-2}D^{\mathrm{II}}}{\left(D^{\mathrm{II}}\right)^2-\left(D^{\mathrm{III}}\right)^2}\int_{\frac{D^{\mathrm{II}}}{2}}^{\frac{D^{\mathrm{III}}}{2}}\left(T_t-T_0\right)\xi \mathrm{d}r}{\frac{D^{\mathrm{II}}\left[\left(D^{\mathrm{II}}\right)^2\left(1-\mu^{-1}\right)+\left(D^{\mathrm{I}}\right)^2\left(1+\mu^{-1}\right)\right]}{2E^{-1}\left[\left(D^{\mathrm{I}}\right)^2-\left(D^{\mathrm{II}}\right)^2\right]} - \frac{D^{\mathrm{II}}\left[\left(D^{\mathrm{II}}\right)^2\left(1-\mu^{-2}\right)+\left(D^{\mathrm{III}}\right)^2\left(1+\mu^{-2}\right)\right]}{2E^{-2}\left[\left(D^{\mathrm{II}}\right)^2-\left(D^{\mathrm{III}}\right)^2\right]}} \tag{7}$$

2.2.2 Structural temperature rise - radial displacement modeling of no-stress edges of rotating ring geometries

Radial displacements of the inner edge of ring geometry 1 and the outer edge of ring geometry 2 (no-stress edges), which are caused by the comprehensive effect of their structural temperature rise T_t - T_0 and interference stress P_{t} , can be obtained respectively according to equation (1) as well:

$$\begin{aligned} u_t^{\mathrm{I}} = & -\frac{4\alpha^{-1}D^{\mathrm{I}}}{\left(D^{\mathrm{I}}\right)^2-\left(D^{\mathrm{II}}\right)^2}\int_{\frac{D^{\mathrm{I}}}{2}}^{\frac{D^{\mathrm{II}}}{2}}\left(T_t-T_0\right)\xi \mathrm{d}r + \frac{D^{\mathrm{I}}\left(D^{\mathrm{II}}\right)^2}{E^{-1}\left[\left(D^{\mathrm{I}}\right)^2-\left(D^{\mathrm{II}}\right)^2\right]}\bullet P_t \\ & +\frac{\rho^{-1}\omega^2 D^{\mathrm{I}}}{64E^{-1}}\left[\left(3+\mu^{-1}\right)\left(1-\mu^{-1}\right)\left(D^{\mathrm{II}}\right)^2+\left(3+\mu^{-1}\right)\left(1-\mu^{-1}\right)\left(D^{\mathrm{I}}\right)^2+\left(D^{\mathrm{II}}\right)^2\left(1+\mu^{-1}\right)\left(3+\mu^{-1}\right)-\left(D^{\mathrm{I}}\right)^2+\left(D^{\mathrm{I}}\right)^2\left(\mu^{-1}\right)^2\right] \end{aligned} \tag{8}$$

$$\begin{aligned} u_t^{\mathrm{III}} = & 2\alpha^{-2}\left\{\frac{\left(1+\mu^{-2}\right)}{D^{\mathrm{III}}} - \frac{\left(D^{\mathrm{II}}\right)^2\left(1+\mu^{-2}\right)}{D^{\mathrm{III}}\left[\left(D^{\mathrm{II}}\right)^2-\left(D^{\mathrm{III}}\right)^2\right]} - \frac{D^{\mathrm{III}}\left(1-\mu^{-2}\right)}{\left(D^{\mathrm{II}}\right)^2-\left(D^{\mathrm{III}}\right)^2}\right\}\int_{\frac{D^{\mathrm{II}}}{2}}^{\frac{D^{\mathrm{III}}}{2}}\left(T_t-T_0\right)\xi \mathrm{d}r - \frac{D^{\mathrm{III}}\left(D^{\mathrm{II}}\right)^2}{E^{-2}\left[\left(D^{\mathrm{II}}\right)^2-\left(D^{\mathrm{III}}\right)^2\right]}\bullet P_t \\ & +\frac{\rho^{-2}\omega^2 D^{\mathrm{III}}}{64E^{-2}}\left[\left(1-\mu^{-2}\right)\left(3+\mu^{-2}\right)\left(D^{\mathrm{II}}\right)^2+\left(1-\mu^{-2}\right)\left(3+\mu^{-2}\right)\left(D^{\mathrm{III}}\right)^2+\left(D^{\mathrm{II}}\right)^2\left(3+\mu^{-2}\right)\left(1+\mu^{-2}\right)-\left(D^{\mathrm{III}}\right)^2+\left(D^{\mathrm{III}}\right)^2\left(\mu^{-2}\right)^2\right] \end{aligned} \tag{9}$$

In equations (8) and (9), P_{t} must be calculated according to the equation (7). Then these conclusions can be the theoretical guidance for the thermal displacement calculations of outer groove (inner edge of outer ring) and inner groove (outer edge of inner ring) of both the short cylindrical roller bearing and angular contact ball bearing in Section 3.

3 Thermal variation modeling of relative ring displacement of typical spindle bearings

Based on the theoretical preparations in Section 2, this section investigates the thermal variation modeling methods of relative ring displacements of short cylindrical roller bearings and angular contact ball bearing. This section introduces the basis for the thermal errors modeling of motorized spindle unit in Section 4. To facilitate theoretical analyses in this section, relative angular locations of rollers in a common bearing structure are defined in Fig. 3. The angular position of each bearing roller and the angular interval between any two neighboring rollers respectively are:

$$\begin{cases} \psi_j = \dfrac{2\pi(j-1)}{Z} \\ \Delta\psi = \dfrac{2\pi}{Z} \end{cases} \tag{10}$$

3.1 Thermal variation modeling of relative ring displacement of short cylindrical roller bearing

Fig. 4 (a) shows the structural and assembly conditions of the short cylindrical roller bearing: The bearing outer ring has concerned diameters $D^{\mathrm{I}}{}_{\mathrm{CO}}$/ $D^{\mathrm{II}}{}_{\mathrm{CO}}$/ $D^{\mathrm{III}}{}_{\mathrm{CO}}$, and there is an interference fit I_{CO} between the outer ring and bearing housing. Similarly, the bearing inner ring has concerned diameters $D^{\mathrm{I}}{}_{\mathrm{CI}}$/ $D^{\mathrm{II}}{}_{\mathrm{CI}}$/ $D^{\mathrm{III}}{}_{\mathrm{CI}}$, and there is an interference fit I_{CI} between the inner ring and shaft. The short cylindrical roller has the d_{C} diameter and l length. On the other hand, as shown in Fig. 4 (b), the short cylindrical roller bearing, operating at an angular velocity ω, will has the radial displacement $\delta_{\mathrm{C\_r}}$, when it is influenced by a radial load $F_{\mathrm{C\_r}}$. Because the short cylindrical roller bearing is designed to allow the relative axial movement between its inner and outer ring to some extent, its load and relative ring displacement on radial direction are considered exclusively. When the short cylindrical roller bearing has a structural temperature rise T_{C_t}-T_0, all of its parts will have thermal deformations causing thermal variation of its relative ring displacement. Therefore, thermal deformations of bearing rollers and the thermal displacements of bearing grooves must be analyzed.

3.1.1 Roller thermal deformation modeling of short cylindrical roller bearing

Thermal deformation calculation methods of the roller, in Fig. 4 (a), of the short cylindrical roller bearing can be described respectively as follows:

$$\begin{cases}\Delta l_t = \alpha_{\mathrm{C}}^{\mathrm{bea}} l_0 \left(T_{\mathrm{C}\_t} - T_0\right) \\ \Delta d_{\mathrm{C}\_t} = \alpha_{\mathrm{C}}^{\mathrm{bea}} d_{\mathrm{C}\_0} \left(T_{\mathrm{C}\_t} - T_0\right)\end{cases} \tag{11}$$

3.1.2 Groove thermal displacement modeling of short cylindrical roller bearing

As illustrated in Fig.4 (a), for the structure of short cylindrical roller bearing, the rollers are contacted with the outer groove (inner edge of outer ring) and inner groove (outer edge of inner ring). Because outer ring - bearing housing and inner ring - spindle shaft are assembled by interference methods respectively, the thermal displacements of the bearing grooves can be calculated based on the thermo-mechanical model of the interference assembled rotating ring geometries in Section 2. For the static outer groove, its thermal displacement is calculated based on ω=0, and it must be determined according to equation (8):

$$u_{\mathrm{CO}\_t}^{\mathrm{I}} = -\frac{4\alpha_{\mathrm{C}}^{\mathrm{bea}} D_{\mathrm{CO}}^{\mathrm{I}}}{\left(D_{\mathrm{CO}}^{\mathrm{I}}\right)^2 - \left(D_{\mathrm{CO}}^{\mathrm{II}}\right)^2} \int_{\frac{D_{\mathrm{CO}}^{\mathrm{I}}}{2}}^{\frac{D_{\mathrm{CO}}^{\mathrm{II}}}{2}} \left(T_{\mathrm{C}\_t} - T_0\right)\xi \mathrm{d}\xi + \frac{D_{\mathrm{CO}}^{\mathrm{I}}\left(D_{\mathrm{CO}}^{\mathrm{II}}\right)^2}{E_{\mathrm{C}}^{\mathrm{bea}}\left[\left(D_{\mathrm{CO}}^{\mathrm{I}}\right)^2 - \left(D_{\mathrm{CO}}^{\mathrm{II}}\right)^2\right]} \bullet P_{\mathrm{CO}\_t} \tag{12}$$

In equation (12), P_{CO_t} is:

$$P_{\mathrm{CO}\_t} = \frac{I_{\mathrm{CO}\_0} + 2\alpha_{\mathrm{C}}^{\mathrm{bea}}\left[\frac{\left(1+\mu_{\mathrm{C}}^{\mathrm{bea}}\right)}{D_{\mathrm{CO}}^{\mathrm{II}}} - \frac{D_{\mathrm{CO}}^{\mathrm{II}}\left(1-\mu_{\mathrm{C}}^{\mathrm{bea}}\right)}{\left(D_{\mathrm{CO}}^{\mathrm{I}}\right)^2 - \left(D_{\mathrm{CO}}^{\mathrm{II}}\right)^2} - \frac{\left(D_{\mathrm{CO}}^{\mathrm{I}}\right)^2\left(1+\mu_{\mathrm{C}}^{\mathrm{bea}}\right)}{D_{\mathrm{CO}}^{\mathrm{II}}\left[\left(D_{\mathrm{CO}}^{\mathrm{I}}\right)^2 - \left(D_{\mathrm{CO}}^{\mathrm{II}}\right)^2\right]}\right]\int_{\frac{D_{\mathrm{CO}}^{\mathrm{I}}}{2}}^{\frac{D_{\mathrm{CO}}^{\mathrm{II}}}{2}}\left(T_{\mathrm{C}\_t} - T_0\right)\xi \mathrm{d}\xi - \frac{4\alpha_{\mathrm{C}}^{\mathrm{hou}} D_{\mathrm{CO}}^{\mathrm{II}}}{\left(D_{\mathrm{CO}}^{\mathrm{II}}\right)^2 - \left(D_{\mathrm{CO}}^{\mathrm{II}}\right)^2}\int_{\frac{D_{\mathrm{CO}}^{\mathrm{II}}}{2}}^{\frac{D_{\mathrm{CO}}^{\mathrm{III}}}{2}}\left(T_{\mathrm{C}\_t} - T_0\right)\xi \mathrm{d}\xi}{\frac{D_{\mathrm{CO}}^{\mathrm{II}}\left[\left(D_{\mathrm{CO}}^{\mathrm{II}}\right)^2\left(1-\mu_{\mathrm{C}}^{\mathrm{bea}}\right) + \left(D_{\mathrm{CO}}^{\mathrm{I}}\right)^2\left(1+\mu_{\mathrm{C}}^{\mathrm{bea}}\right)\right]}{2E_{\mathrm{C}}^{\mathrm{bea}}\left[\left(D_{\mathrm{CO}}^{\mathrm{I}}\right)^2 - \left(D_{\mathrm{CO}}^{\mathrm{II}}\right)^2\right]} - \frac{D_{\mathrm{CO}}^{\mathrm{II}}\left[\left(D_{\mathrm{CO}}^{\mathrm{II}}\right)^2\left(1-\mu_{\mathrm{C}}^{\mathrm{hou}}\right) + \left(D_{\mathrm{CO}}^{\mathrm{III}}\right)^2\left(1+\mu_{\mathrm{C}}^{\mathrm{hou}}\right)\right]}{2E_{\mathrm{C}}^{\mathrm{hou}}\left[\left(D_{\mathrm{CO}}^{\mathrm{II}}\right)^2 - \left(D_{\mathrm{CO}}^{\mathrm{III}}\right)^2\right]}} \tag{13}$$

Unlike the outer ring, the thermal displacement of rotating inner groove can be determined according to equation (9):

$$u_{\mathrm{CI}\_t}^{\mathrm{III}}=2\alpha_{\mathrm{C}}^{\mathrm{bea}}\left[\frac{\left(1+\mu_{\mathrm{C}}^{\mathrm{bea}}\right)}{D_{\mathrm{CI}}^{\mathrm{III}}}-\frac{D_{\mathrm{CI}}^{\mathrm{II}\,2}\left(1+\mu_{\mathrm{C}}^{\mathrm{bea}}\right)}{D_{\mathrm{CI}}^{\mathrm{III}}\left[\left(D_{\mathrm{CI}}^{\mathrm{II}}\right)^2-\left(D_{\mathrm{CI}}^{\mathrm{III}}\right)^2\right]}-\frac{D_{\mathrm{CI}}^{\mathrm{III}}\left(1-\mu_{\mathrm{C}}^{\mathrm{bea}}\right)}{\left(D_{\mathrm{CI}}^{\mathrm{II}}\right)^2-\left(D_{\mathrm{CI}}^{\mathrm{III}}\right)^2}\right]\int_{\frac{D_{\mathrm{CI}}^{\mathrm{II}}}{2}}^{\frac{D_{\mathrm{CI}}^{\mathrm{III}}}{2}}\left(T_{\mathrm{C}\_t}-T_0\right)\xi\,\mathrm{d}\xi-\frac{D_{\mathrm{CI}}^{\mathrm{III}}\left(D_{\mathrm{CI}}^{\mathrm{II}}\right)^2}{E_{\mathrm{C}}^{\mathrm{bea}}\left[\left(D_{\mathrm{CI}}^{\mathrm{II}}\right)^2-\left(D_{\mathrm{CI}}^{\mathrm{III}}\right)^2\right]}\bullet P_{\mathrm{CI}\_t}$$

$$+\frac{\rho_{\mathrm{C}}^{\mathrm{bea}}\omega^2 D_{\mathrm{CI}}^{\mathrm{III}}}{64E_{\mathrm{C}}^{\mathrm{bea}}}\left[\left(1-\mu_{\mathrm{C}}^{\mathrm{bea}}\right)\left(3+\mu_{\mathrm{C}}^{\mathrm{bea}}\right)\left(D_{\mathrm{CI}}^{\mathrm{II}}\right)^2+\left(1-\mu_{\mathrm{C}}^{\mathrm{bea}}\right)\left(3+\mu_{\mathrm{C}}^{\mathrm{bea}}\right)\left(D_{\mathrm{CI}}^{\mathrm{III}}\right)^2+\left(D_{\mathrm{CI}}^{\mathrm{II}}\right)^2\left(3+\mu_{\mathrm{C}}^{\mathrm{bea}}\right)\left(1+\mu_{\mathrm{C}}^{\mathrm{bea}}\right)-\left(D_{\mathrm{CI}}^{\mathrm{III}}\right)^2+\left(D_{\mathrm{CI}}^{\mathrm{III}}\right)^2\left(\mu_{\mathrm{C}}^{\mathrm{bea}}\right)^2\right] \quad (14)$$

In equation (14), P_{CI_t} is:

$$P_{\mathrm{CI}\_t}=\frac{I_{\mathrm{CI}\_0}+2\alpha^{\mathrm{spi}}\left[\frac{\left(1+\mu^{\mathrm{spi}}\right)}{D_{\mathrm{CI}}^{\mathrm{II}}}-\frac{D_{\mathrm{CI}}^{\mathrm{II}}\left(1-\mu^{\mathrm{spi}}\right)}{\left(D_{\mathrm{CI}}^{\mathrm{I}}\right)^2-\left(D_{\mathrm{CI}}^{\mathrm{II}}\right)^2}-\frac{\left(D_{\mathrm{CI}}^{\mathrm{I}}\right)^2\left(1+\mu^{\mathrm{spi}}\right)}{D_{\mathrm{CI}}^{\mathrm{II}}\left[\left(D_{\mathrm{CI}}^{\mathrm{I}}\right)^2-\left(D_{\mathrm{CI}}^{\mathrm{II}}\right)^2\right]}\right]\int_{\frac{D_{\mathrm{CI}}^{\mathrm{I}}}{2}}^{\frac{D_{\mathrm{CI}}^{\mathrm{II}}}{2}}\left(T_{\mathrm{C}\_t}-T_0\right)\xi\,\mathrm{d}\xi-\frac{4\alpha_{\mathrm{C}}^{\mathrm{bea}}D_{\mathrm{CI}}^{\mathrm{II}}}{\left(D_{\mathrm{CI}}^{\mathrm{II}}\right)^2-\left(D_{\mathrm{CI}}^{\mathrm{III}}\right)^2}\int_{\frac{D_{\mathrm{CI}}^{\mathrm{II}}}{2}}^{\frac{D_{\mathrm{CI}}^{\mathrm{III}}}{2}}\left(T_{\mathrm{C}\_t}-T_0\right)\xi\,\mathrm{d}\xi}{\frac{D_{\mathrm{CI}}^{\mathrm{II}}\left[\left(D_{\mathrm{CI}}^{\mathrm{II}}\right)^2\left(1-\mu^{\mathrm{spi}}\right)+\left(D_{\mathrm{CI}}^{\mathrm{I}}\right)^2\left(1+\mu^{\mathrm{spi}}\right)\right]}{2E^{\mathrm{spi}}\left[\left(D_{\mathrm{CI}}^{\mathrm{I}}\right)^2-\left(D_{\mathrm{CI}}^{\mathrm{II}}\right)^2\right]}-\frac{D_{\mathrm{CI}}^{\mathrm{II}}\left[\left(D_{\mathrm{CI}}^{\mathrm{II}}\right)^2\left(1-\mu_{\mathrm{C}}^{\mathrm{bea}}\right)+\left(D_{\mathrm{CI}}^{\mathrm{III}}\right)^2\left(1+\mu_{\mathrm{C}}^{\mathrm{bea}}\right)\right]}{2E_{\mathrm{C}}^{\mathrm{bea}}\left[\left(D_{\mathrm{CI}}^{\mathrm{II}}\right)^2-\left(D_{\mathrm{CI}}^{\mathrm{III}}\right)^2\right]}} \quad (15)$$

3.1.3 Thermal variation modeling of relative ring displacement of short cylindrical roller bearing

Models of thermal deformations of bearing rollers and the thermal displacements of bearing grooves can be adopted to analyze the thermal variation of relative ring displacement of short cylindrical roller bearing. When the operating short cylindrical roller bearing is under a radial force $F_{\mathrm{C\_r}}$ shown in Fig. 4 (b), the force balance relationship of the j^{th} cylindrical roller of the bearing at moment t is shown in Fig. 5. According to the theoretical method about short cylindrical roller bearing in classical book [21], the force balance equation of operating short cylindrical roller bearing can be:

$$\frac{F_{\mathrm{C}\_r}}{8.05\times10^4\left(\Delta l_t+l_0\right)^{\frac{8}{9}}}-\sum_{j=1}^{j=Z}\delta_{\mathrm{C}ij\_t}^{\frac{10}{9}}\cos\psi_j=0 \quad (16)$$

Besides, the force balance equation of j^{th} cylindrical roller of the bearing can be:

$$\left[\left(\delta_{\text{Cr}\_t}\cos\psi_j-\frac{P_{\text{dC}\_0}+2u^{\text{I}}_{\text{CO}\_t}+2u^{\text{III}}_{\text{CI}\_t}-\Delta d_{\text{C}\_t}}{2}-\delta_{\text{C}ij\_t}\right)^{\frac{10}{9}}-\delta_{\text{C}ij\_t}^{\frac{10}{9}}\right]-\frac{F^{\text{cen}}_{\text{C}j\_t}}{8.05\times10^{4}\left(\Delta l_t+l_0\right)^{\frac{8}{9}}}=0 \tag{17}$$

In equation (17), $\Delta d_{\text{C}\_t}/\Delta l_t$ must be calculated according to equations (11), and $u^{\text{I}}_{\text{CO}\_t}/u^{\text{III}}_{\text{CI}\_t}$ are determined by equations (12) and (14) respectively. The roller centrifugal force $F^{\text{cen}}_{\text{C}j\_t}$ should be calculated by the method:

$$F^{\text{cen}}_{\text{C}j\_t}=3.39\times10^{-11}\left(d_{\text{C}\_0}+\Delta d_{\text{C}\_t}\right)^2\left(l_0+\Delta l_t\right)d_{\text{m}\_\text{C}}n_m^{\ 2} \tag{18}$$

The solution of simultaneous equations (16) and (17) are solved by Newton - Raphson method for δ_{Cr_t}. After solutions, the variation of relative ring displacement of short cylindrical roller bearing due to its temperature rise $T_{\text{C}\_t}-T_0$ has to be calculated by the following method:

$$\left.\overline{\delta_{\text{C}\_\text{r}}}\right|_{T_{\text{C}\_t}-T_0}=\delta_{\text{Cr}\_t}-\delta_{\text{Cr}\_0} \tag{19}$$

3.2 Thermal variation modeling of relative ring displacement of angular contact ball bearing

The structural and assembly conditions of angular contact ball bearing are almost similar with short cylindrical roller bearing. As depicted in Fig. 6 (a), the bearing outer ring has concerned diameters D^{I}_{AO}/ $D^{\text{II}}_{\text{AO}}$/ $D^{\text{III}}_{\text{AO}}$, and there is an interference fit I_{AO} between the outer ring and bearing housing. The bearing inner ring has concerned diameters D^{I}_{AI}/ $D^{\text{II}}_{\text{AI}}$/ $D^{\text{III}}_{\text{AI}}$, and there is an interference fit I_{AI} between the inner ring and spindle shaft. Besides, Fig. 6 (b) shows some detail bearing parameters for the ball roller - bearing ring contacts: The diameter of the ball roller is d_{A}. The bearing inner and outer ring has the groove length/ radius l_{i}/ r_{i} and l_{o}/ r_{o} respectively. The angular contact ball bearing without external load has the initial contact angle α. The central distance between outer and inner grooves is A. Specially, the scales of D^{I}_{AO} and $D^{\text{III}}_{\text{AI}}$ in Fig. 6 (a) must be analyzed in detail to be 6 bearing diameters ($D^{\mathrm{I}-i}_{\mathrm{AO}}$ and $D^{\mathrm{III}-i}_{\mathrm{AI}}$, i=1,2,3) in Fig. 6 (b). The locations 3 and 1' are the deepest positions of outer and inner grooves respectively. Fig. 6 (c) reveals the bearing load and displacement conditions: Generally, the angular contact ball bearing, operating at an angular velocity ω, will have the radial displacement $\delta_{\mathrm{A\_r}}$ /axial displacement $\delta_{\mathrm{A\_a}}$ /angular displacement θ, which are caused by the bearing radial load $F_{\mathrm{A\_r}}$ /axial load $F_{\mathrm{A\_a}}$ /torque M_{A} respectively. When the angular contact ball bearing has a structural temperature rise T_{A_t}-T_0, all the bearing parts will have thermal deformations, and then causes the thermal variations of its radial/ axial/ angular relative ring displacement. Therefore, thermal deformations of bearing rollers and thermal displacements of bearing grooves must be calculated.

3.2.1 Roller thermal deformation modeling of angular contact ball bearing

As depicted in Fig. 6 (a), the roller of angular contact ball bearing is contacted with its outer and inner groove. Then the thermal deformation of outer/ inner groove width and ball roller diameter, shown in Fig. 6 (b), can be calculated respectively as follows:

$$\Delta l_{\mathrm{o(i)}\_t} = \alpha_{\mathrm{A}}^{\mathrm{bea}} l_{\mathrm{o(i)\_0}} \left(T_{\mathrm{A}\_t} - T_0\right) \tag{20}$$

$$\Delta d_{\mathrm{A}\_t} = \alpha_{\mathrm{A}}^{\mathrm{bea}} d_{\mathrm{A\_0}} \left(T_{\mathrm{A}\_t} - T_0\right) \tag{21}$$

3.2.2 Groove thermal displacement modeling of angular contact ball bearing

Being similar with the short cylindrical roller bearing, angular contact ball bearing has 2 part pairs assembled by interference method respectively: outer ring - bearing housing and inner ring - spindle shaft, which is shown in Fig. 6 (a). The rollers are contacted with the outer groove (inner edge of outer ring) and inner groove (outer edge of inner ring). The thermal displacements of bearing groove positions can be gained by thermo-mechanical model of the interference assembled rotating ring geometries in Section 2. According to equation (8), thermal displacements of positions 1, 2, 3 of static outer groove, shown in Fig. 6 (b), caused by temperature rise T_{A_t}-T_0 of angular contact ball bearing can be calculated based on ω=0:

$$u_{\mathrm{AO\_}t}^{\mathrm{I\_}i} = -\frac{4\alpha_{\mathrm{A}}^{\mathrm{bea}} D_{\mathrm{AO}}^{\mathrm{I\_}i}}{\left(D_{\mathrm{AO}}^{\mathrm{I\_}i}\right)^2 - \left(D_{\mathrm{AO}}^{\mathrm{II}}\right)^2} \int_{\frac{D_{\mathrm{AO}}^{\mathrm{I\_}i}}{2}}^{\frac{D_{\mathrm{AO}}^{\mathrm{II}}}{2}} \left(T_{\mathrm{A\_}t} - T_0\right)\xi \mathrm{d}\xi + \frac{D_{\mathrm{AO}}^{\mathrm{I\_}i}\left(D_{\mathrm{AO}}^{\mathrm{II}}\right)^2}{E_{\mathrm{A}}^{\mathrm{bea}}\left[\left(D_{\mathrm{AO}}^{\mathrm{I\_}i}\right)^2 - \left(D_{\mathrm{AO}}^{\mathrm{II}}\right)^2\right]} \bullet P_{\mathrm{AO\_}t}, i = 1,2,3 \qquad (22)$$

In equation (22), $P_{\mathrm{AO\_}t}$ is:

$$P_{\mathrm{AO\_}t} = \frac{I_{\mathrm{AO\_0}} + 2\alpha_{\mathrm{A}}^{\mathrm{bea}}\left[\frac{\left(1+\mu_{\mathrm{A}}^{\mathrm{bea}}\right)}{D_{\mathrm{AO}}^{\mathrm{II}}} - \frac{D_{\mathrm{AO}}^{\mathrm{II}}\left(1-\mu_{\mathrm{A}}^{\mathrm{bea}}\right)}{\left(D_{\mathrm{AO}}^{\mathrm{I\_}i}\right)^2 - \left(D_{\mathrm{AO}}^{\mathrm{II}}\right)^2} - \frac{\left(D_{\mathrm{AO}}^{\mathrm{I\_}i}\right)^2\left(1+\mu_{\mathrm{A}}^{\mathrm{bea}}\right)}{D_{\mathrm{AO}}^{\mathrm{II}}\left[\left(D_{\mathrm{AO}}^{\mathrm{I\_}i}\right)^2 - \left(D_{\mathrm{AO}}^{\mathrm{II}}\right)^2\right]}\right]\int_{\frac{D_{\mathrm{AO}}^{\mathrm{I\_}i}}{2}}^{\frac{D_{\mathrm{AO}}^{\mathrm{II}}}{2}}\left(T_{\mathrm{A\_}t} - T_0\right)\xi \mathrm{d}r - \frac{4\alpha_{\mathrm{A}}^{\mathrm{hou}} D_{\mathrm{AO}}^{\mathrm{II}}}{\left(D_{\mathrm{AO}}^{\mathrm{II}}\right)^2 - \left(D_{\mathrm{AO}}^{\mathrm{III}}\right)^2}\int_{\frac{D_{\mathrm{AO}}^{\mathrm{II}}}{2}}^{\frac{D_{\mathrm{AO}}^{\mathrm{III}}}{2}}\left(T_{\mathrm{A\_}t} - T_0\right)\xi \mathrm{d}r}{\frac{D_{\mathrm{AO}}^{\mathrm{II}}\left[\left(D_{\mathrm{AO}}^{\mathrm{II}}\right)^2\left(1-\mu_{\mathrm{A}}^{\mathrm{bea}}\right) + \left(D_{\mathrm{AO}}^{\mathrm{I\_}i}\right)^2\left(1+\mu_{\mathrm{A}}^{\mathrm{bea}}\right)\right]}{2E_{\mathrm{A}}^{\mathrm{bea}}\left[\left(D_{\mathrm{AO}}^{\mathrm{I\_}i}\right)^2 - \left(D_{\mathrm{AO}}^{\mathrm{II}}\right)^2\right]} - \frac{D_{\mathrm{AO}}^{\mathrm{II}}\left[\left(D_{\mathrm{AO}}^{\mathrm{II}}\right)^2\left(1-\mu_{\mathrm{A}}^{\mathrm{hou}}\right) + \left(D_{\mathrm{AO}}^{\mathrm{III}}\right)^2\left(1+\mu_{\mathrm{A}}^{\mathrm{hou}}\right)\right]}{2E_{\mathrm{A}}^{\mathrm{hou}}\left[\left(D_{\mathrm{AO}}^{\mathrm{II}}\right)^2 - \left(D_{\mathrm{AO}}^{\mathrm{III}}\right)^2\right]}}$$
$$, i = 1,2,3 \qquad (23)$$

Meanwhile, thermal displacements of positions 1', 2', 3' of rotating inner groove in Fig. 6 (b) can be gained according to equation (9) as well:

$$u_{\mathrm{AI\_}t}^{\mathrm{III\_}i} = 2\alpha_{\mathrm{A}}^{\mathrm{bea}}\left\{\frac{\left(1+\mu_{\mathrm{A}}^{\mathrm{bea}}\right)}{D_{\mathrm{AI}}^{\mathrm{III\_}i}} - \frac{\left(D_{\mathrm{AI}}^{\mathrm{II}}\right)^2\left(1+\mu_{\mathrm{A}}^{\mathrm{bea}}\right)}{D_{\mathrm{AI}}^{\mathrm{III\_}i}\left[\left(D_{\mathrm{AI}}^{\mathrm{II}}\right)^2 - \left(D_{\mathrm{AI}}^{\mathrm{III\_}i}\right)^2\right]} - \frac{D_{\mathrm{AI}}^{\mathrm{III\_}i}\left(1-\mu_{\mathrm{A}}^{\mathrm{bea}}\right)}{\left(D_{\mathrm{AI}}^{\mathrm{II}}\right)^2 - \left(D_{\mathrm{AI}}^{\mathrm{III\_}i}\right)^2}\right\}\int_{\frac{D_{\mathrm{AI}}^{\mathrm{II}}}{2}}^{\frac{D_{\mathrm{AI}}^{\mathrm{III\_}i}}{2}}\left(T_{\mathrm{A\_}t} - T_0\right)\xi \mathrm{d}r - \frac{D_{\mathrm{AI}}^{\mathrm{III\_}i}\left(D_{\mathrm{AI}}^{\mathrm{II}}\right)^2}{E_{\mathrm{A}}^{\mathrm{bea}}\left[\left(D_{\mathrm{AI}}^{\mathrm{II}}\right)^2 - \left(D_{\mathrm{AI}}^{\mathrm{III\_}i}\right)^2\right]} \bullet P_{\mathrm{AI\_}t}$$
$$+\frac{\rho_{\mathrm{A}}^{\mathrm{bea}}\omega^2 D_{\mathrm{AI}}^{\mathrm{III\_}i}}{64E_{\mathrm{A}}^{\mathrm{bea}}}\left[\left(1-\mu_{\mathrm{A}}^{\mathrm{bea}}\right)\left(3+\mu_{\mathrm{A}}^{\mathrm{bea}}\right)\left(D_{\mathrm{AI}}^{\mathrm{II}}\right)^2 + \left(1-\mu_{\mathrm{A}}^{\mathrm{bea}}\right)\left(3+\mu_{\mathrm{A}}^{\mathrm{bea}}\right)\left(D_{\mathrm{AI}}^{\mathrm{III\_}i}\right)^2 + \left(D_{\mathrm{AI}}^{\mathrm{II}}\right)^2\left(3+\mu_{\mathrm{A}}^{\mathrm{bea}}\right)\left(1+\mu_{\mathrm{A}}^{\mathrm{bea}}\right) - \left(D_{\mathrm{AI}}^{\mathrm{III\_}i}\right)^2 + \left(D_{\mathrm{AI}}^{\mathrm{III\_}i}\right)^2\left(\mu_{\mathrm{A}}^{\mathrm{bea}}\right)^2\right]$$
$$, i = 1', 2', 3' \qquad (24)$$

In equation (24), $P_{\mathrm{AI\_}t}$ is:

$$P_{\mathrm{AI\_}t} = \frac{I_{\mathrm{AI\_0}} + 2\alpha^{\mathrm{spi}}\left[\frac{\left(1+\mu^{\mathrm{spi}}\right)}{D_{\mathrm{AI}}^{\mathrm{II}}} - \frac{D_{\mathrm{AI}}^{\mathrm{II}}\left(1-\mu^{\mathrm{spi}}\right)}{\left(D_{\mathrm{AI}}^{\mathrm{I}}\right)^2 - \left(D_{\mathrm{AI}}^{\mathrm{II}}\right)^2} - \frac{\left(D_{\mathrm{AI}}^{\mathrm{I}}\right)^2\left(1+\mu^{\mathrm{spi}}\right)}{D_{\mathrm{AI}}^{\mathrm{II}}\left[\left(D_{\mathrm{AI}}^{\mathrm{I}}\right)^2 - \left(D_{\mathrm{AI}}^{\mathrm{II}}\right)^2\right]}\right]\int_{\frac{D_{\mathrm{AI}}^{\mathrm{I}}}{2}}^{\frac{D_{\mathrm{AI}}^{\mathrm{II}}}{2}}\left(T_{\mathrm{A\_}t} - T_0\right)\xi \mathrm{d}r - \frac{4\alpha_{\mathrm{A}}^{\mathrm{bea}} D_{\mathrm{AI}}^{\mathrm{II}}}{\left(D_{\mathrm{AI}}^{\mathrm{II}}\right)^2 - \left(D_{\mathrm{AI}}^{\mathrm{III\_}i}\right)^2}\int_{\frac{D_{\mathrm{AI}}^{\mathrm{II}}}{2}}^{\frac{D_{\mathrm{AI}}^{\mathrm{III\_}i}}{2}}\left(T_{\mathrm{A\_}t} - T_0\right)\xi \mathrm{d}r}{\frac{D_{\mathrm{AI}}^{\mathrm{II}}\left[\left(D_{\mathrm{AI}}^{\mathrm{II}}\right)^2\left(1-\mu^{\mathrm{spi}}\right) + \left(D_{\mathrm{AI}}^{\mathrm{I}}\right)^2\left(1+\mu^{\mathrm{spi}}\right)\right]}{2E^{\mathrm{spi}}\left[\left(D_{\mathrm{AI}}^{\mathrm{I}}\right)^2 - \left(D_{\mathrm{AI}}^{\mathrm{II}}\right)^2\right]} - \frac{D_{\mathrm{AI}}^{\mathrm{II}}\left[\left(D_{\mathrm{AI}}^{\mathrm{II}}\right)^2\left(1-\mu_{\mathrm{A}}^{\mathrm{bea}}\right) + \left(D_{\mathrm{AI}}^{\mathrm{III\_}i}\right)^2\left(1+\mu_{\mathrm{A}}^{\mathrm{bea}}\right)\right]}{2E_{\mathrm{A}}^{\mathrm{bea}}\left[\left(D_{\mathrm{AI}}^{\mathrm{II}}\right)^2 - \left(D_{\mathrm{AI}}^{\mathrm{III\_}i}\right)^2\right]}}$$
$$, i = 1', 2', 3' \qquad (25)$$

3.2.3 Thermal variation modeling of initial contact angle of angular contact ball bearing

The roller thermal deformation and groove thermal displacement models can be used to analyze the thermal variation of initial contact angle of angular contact ball bearing. If an angular contact ball bearing without external load has a structural temperature rise T_{A_t}-T_0, the thermal drifts of bearing groove radii and ball roller diameters will cause the thermal variation of bearing initial contact angle, and then cause the relative ring displacements of angular contact ball bearing. As demonstrated in Fig. 7(a) and (b), the curvature centers of bearing inner and outer grooves are placed onto the origin of coordinate system respectively. The bearing structural temperature change T_{A_t}-T_0 leads to its contour thermal variation of inner and outer rings and center thermal shift of bearing grooves. The coordinates of initial positions 1, 2, 3 of bearing outer groove in Fig. 7 (a) meet a relationship:

$$x^2 + y^2 = r_{\mathrm{o}\_0}^2 \tag{26}$$

Then varying locations of these 3 positions (1*, 2*, 3*), owing to the groove thermal drift, meet:

$$\left(x - u_{\mathrm{ox}\_t}\right) + \left(y - u_{\mathrm{oy}\_t}\right) = r_{\mathrm{o}\_t}^2 \tag{27}$$

Then the coordinate transformations from positions 1, 2, 3 to 1*, 2*, 3* can be:

$$\left(x_{i*}, y_{i*}\right) = \left(x_i + u_{xi\_t}, y_i + u_{yi\_t}\right) = \left(x_i + \frac{x_i \Delta l_{\mathrm{o}\_t}}{x_1 - x_2}, y_i + u_{\mathrm{AO}\_t}^{\mathrm{I}\_i}\right), i = 1, 2, 3 \tag{28}$$

In equation (28), Δl_{o_t} and $u_{\mathrm{AO}\_t}^{\mathrm{I}\_i}$ (i=1, 2, 3) must be obtained according to equations (20) and (22) respectively. Then equation (28) is substituted into (27), and can be simultaneous with equation (26) to solve r_{o_t}. By the same method, r_{i_t} in Fig. 7 (b) can also be gained. Based on these preparations, the initial contact angle of angular contact ball bearing can be obtained according to geometry relationship in Fig. 6 (b). By the method introduced in classical book [21], the initial contact angle of angular contact ball bearing can be modeled to be associated with thermal factors:

$$\alpha_t = \cos^{-1}\left[1 - \frac{D_{\mathrm{AO}}^{\mathrm{I\_3}} - D_{\mathrm{AI}}^{\mathrm{III\_1}} + 2\left(u_{\mathrm{AO\_}t}^{\mathrm{I\_3}} - u_{\mathrm{AI\_}t}^{\mathrm{III\_1}} - d_{\mathrm{A\_0}} - \Delta d_{\mathrm{A\_}t}\right)}{2\left(r_{\mathrm{o\_}t} + r_{\mathrm{i\_}t} - d_{\mathrm{A\_0}} - \Delta d_{\mathrm{A\_}t}\right)}\right] \tag{29}$$

In equation (29), $\Delta d_{\mathrm{A\_}t}$, $u_{\mathrm{AO\_}t}^{\mathrm{I\_3}}$ and $u_{\mathrm{AI\_}t}^{\mathrm{III\_1}}$ must be obtained by equations (21), (22) and (24) respectively.

3.2.4 Thermal variation modeling of relative ring axial/ radial/ angular displacements of angular contact ball bearing

On the basis of thermal variation modeling of initial contact angle of angular contact ball bearing, the thermal variation model of relative ring axial/ radial/ angular displacements of angular contact ball bearing can be established based on its defined external axial, radial and angular loads. When the angular contact ball bearing in Fig. 6 (c) is operating with its axial load $F_{\mathrm{A\_a}}$, radial load $F_{\mathrm{A\_r}}$ and torque M_{A}, the position relationship of roller center and curvature centers of bearing outer and inner grooves will be different from its no-load condition.

As illustrated in Fig. 8, for *j*th bearing ball roller, the connecting line of inner and outer ring groove centers is collinear with $Bd_{\mathrm{A}}(A)$ at no-load condition. However, when the angular contact ball bearing is operating with external loads, the connecting line above is no longer collinear with $Bd_{\mathrm{A}}(A)$. This is because the roller centrifugal force results in the contact angle change of angular contact ball bearing. Since the bearing outer ring is generally considered to be fixed in motorized spindle unit, both the curvature center of bearing inner groove and the center of ball roller center are considered to have relative movements to the curvature center of bearing outer groove. By the method introduced in classical book [21], firstly, the geometry relationships in Fig. 8 can be summarized as follows:

$$\begin{cases} \left[\left(r_{\mathrm{i\_}t} + r_{\mathrm{o\_}t} - d_{\mathrm{A\_0}} - \Delta d_{\mathrm{A\_}t}\right)\sin\alpha_t + \delta_{\mathrm{Aa\_}t} + \theta_t \Re_{\mathrm{i}} \cos\Psi_j - X_{1j\_t}\right]^2 + \left(A_{2j\_t} - X_{2j\_t}\right)^2 - \left[r_{\mathrm{i\_}t} - \frac{1}{2}\left(d_{\mathrm{A\_0}} + \Delta d_{\mathrm{A\_}t}\right) + \delta_{\mathrm{Aij\_}t}\right]^2 = 0 \\ X_{1j\_t}{}^2 + X_{2j\_t}{}^2 - \left[r_{\mathrm{o\_}t} - \frac{1}{2}\left(d_{\mathrm{A\_0}} + \Delta d_{\mathrm{A\_}t}\right) + \delta_{\mathrm{Aoj\_}t}\right]^2 = 0 \end{cases} \tag{30}$$

Meanwhile, the force balance relationship of jth ball roller of angular contact ball bearing is shown in Fig. 9. This relationship can be:

$$\begin{cases} \dfrac{2.15\times10^{5}\left(\dfrac{1}{r_{\mathrm{ij}\_t}}+\dfrac{2}{d_{\mathrm{A}\_0}+\Delta d_{\mathrm{A}\_t}}\right)^{-\frac{1}{2}}\left(\delta^{*}\right)^{-\frac{3}{2}}\delta_{\mathrm{Aij}\_t}^{\frac{3}{2}}\left(A_{1j\_t}-X_{1j\_t}\right)}{r_{\mathrm{i}\_t}-\dfrac{1}{2}\left(d_{\mathrm{A}\_0}+\Delta d_{\mathrm{A}\_t}\right)+\delta_{\mathrm{Aij}\_t}} \\ =\dfrac{2.15\times10^{5}\left(\dfrac{1}{r_{\mathrm{oj}\_t}}+\dfrac{2}{d_{\mathrm{A}\_0}+\Delta d_{\mathrm{A}\_t}}\right)^{-\frac{1}{2}}\left(\delta^{*}\right)^{-\frac{3}{2}}\delta_{\mathrm{Aoj}\_t}^{\frac{3}{2}}X_{1j\_t}-\dfrac{2X_{2j\_t}M_{\mathrm{g}j\_t}}{d_{\mathrm{A}\_0}+\Delta d_{\mathrm{A}\_t}}}{r_{\mathrm{o}\_t}-\dfrac{1}{2}\left(d_{\mathrm{A}\_0}+\Delta d_{\mathrm{A}\_t}\right)+\delta_{\mathrm{Aoj}\_t}} \\ \dfrac{2.15\times10^{5}\left(\dfrac{1}{r_{\mathrm{ij}\_t}}+\dfrac{2}{d_{\mathrm{A}\_0}+\Delta d_{\mathrm{A}\_t}}\right)^{-\frac{1}{2}}\left(\delta^{*}\right)^{-\frac{3}{2}}\delta_{\mathrm{Aij}\_t}^{\frac{3}{2}}\left(A_{2j\_t}-X_{2j\_t}\right)}{r_{\mathrm{i}\_t}-\dfrac{1}{2}\left(d_{\mathrm{A}\_0}+\Delta d_{\mathrm{A}\_t}\right)+\delta_{\mathrm{Aij}\_t}}+F_{\mathrm{A}j\_t}^{\mathrm{cen}} \\ =\dfrac{2.15\times10^{5}\left(\dfrac{1}{r_{\mathrm{oj}\_t}}+\dfrac{2}{d_{\mathrm{A}\_0}+\Delta d_{\mathrm{A}\_t}}\right)^{-\frac{1}{2}}\left(\delta^{*}\right)^{-\frac{3}{2}}\delta_{\mathrm{Aoj}\_t}^{\frac{3}{2}}X_{2j\_t}-\dfrac{2M_{\mathrm{g}j\_t}X_{1j\_t}}{d_{\mathrm{A}\_0}+\Delta d_{\mathrm{A}\_t}}}{r_{\mathrm{o}\_t}-\dfrac{1}{2}\left(d_{\mathrm{A}\_0}+\Delta d_{\mathrm{A}\_t}\right)+\delta_{\mathrm{Aoj}\_t}} \end{cases} \quad (31)$$

In equation (31), the centrifugal force $F_{\mathrm{A}j\_t}^{\mathrm{cen}}$ and gyroscopic moment $M_{\mathrm{g}j\_t}$ should be calculated respectively according to following methods:

$$F_{\mathrm{A}j}^{\mathrm{cen}}=\frac{1}{2}m_{\mathrm{A}}d_{\mathrm{m}\_\mathrm{A}}\left(\omega_{\mathrm{i}}\right)^{2}\left(\frac{\omega}{\omega_{\mathrm{i}}}\right)_{j}^{2} \quad (32)$$

$$M_{\mathrm{g}j}=J\left(\frac{\omega_{\mathrm{R}}}{\omega_{\mathrm{i}}}\right)_{j}\left(\frac{\omega_{\mathrm{m}}}{\omega_{\mathrm{i}}}\right)_{j}\left(\omega_{\mathrm{i}}\right)^{2}\sin\beta \quad (33)$$

Simultaneous equations (30) and (31) must be solved by Newton- Raphson method to determine X_{1j_t}/ X_{2j_t}/ δ_{Aij_t}/ δ_{Aoj_t}. Furthermore, to calculate δ_{Ar_t}/ δ_{Aa_t}/ θ_t based on X_{1j_t}/ X_{2j_t}/ δ_{ij_t}/ δ_{oj_t} , simultaneous equations (34) and (35), which are established for force balance analyses onto the angular contact ball bearing as a whole, must be solved:

$$\begin{cases} F_{\mathrm{A\_a}} = 2.15\times10^{5}\sum_{j=1}^{j=Z}\dfrac{\left(A_{1j\_t}-X_{1j\_t}\right)\left(\dfrac{1}{r_{\mathrm{ij}\_t}}+\dfrac{2}{d_{\mathrm{A\_0}}+\Delta d_{\mathrm{A}\_t}}\right)^{-\frac{1}{2}}\left(\delta^{*}\right)^{-\frac{3}{2}}\delta_{\mathrm{Aij}\_t}^{\frac{3}{2}}}{r_{\mathrm{i}\_t}-\dfrac{1}{2}\left(d_{\mathrm{A\_0}}+\Delta d_{\mathrm{A}\_t}\right)+\delta_{\mathrm{Aij}\_t}} \\ F_{\mathrm{A\_r}} = 2.15\times10^{5}\sum_{j=1}^{j=Z}\dfrac{\left(A_{2j\_t}-X_{2j\_t}\right)\left(\dfrac{1}{r_{\mathrm{ij}\_t}}+\dfrac{2}{d_{\mathrm{A\_0}}+\Delta d_{\mathrm{A}\_t}}\right)^{-\frac{1}{2}}\left(\delta^{*}\right)^{-\frac{3}{2}}\delta_{\mathrm{Aij}\_t}^{\frac{3}{2}}\cos\psi_{j}}{r_{\mathrm{i}\_t}-\dfrac{1}{2}\left(d_{\mathrm{A\_0}}+\Delta d_{\mathrm{A}\_t}\right)+\delta_{\mathrm{Aij}\_t}} \\ M_{\mathrm{A}} = 2.15\times10^{5}\sum_{j=1}^{j=Z}\dfrac{\left(A_{1j\_t}-X_{1j\_t}\right)\left(\dfrac{1}{r_{\mathrm{ij}\_t}}+\dfrac{2}{d_{\mathrm{A\_0}}+\Delta d_{\mathrm{A}\_t}}\right)^{-\frac{1}{2}}\left(\delta^{*}\right)^{-\frac{3}{2}}\delta_{\mathrm{Aij}\_t}^{\frac{3}{2}}\Re_{\mathrm{i}}\cos\psi_{j}}{r_{\mathrm{i}\_t}-\dfrac{1}{2}\left(d_{\mathrm{A\_0}}+\Delta d_{\mathrm{A}\_t}\right)+\delta_{\mathrm{Aij}\_t}} \end{cases} \quad (34)$$

In equation (34), $\Re_{\mathrm{i}}$ is the orbit radius of inner groove curvature center of the angular contact ball bearing. It must be determined by:

$$\Re_{\mathrm{i}} = \frac{1}{2}d_{\mathrm{m\_A}} + \left(f_{\mathrm{i}}-0.5\right)d_{\mathrm{A}\_t}\cos\alpha_{t} = \frac{\left(D_{\mathrm{AO}}^{\mathrm{I\_3}}+D_{\mathrm{AI}}^{\mathrm{III\_1}}\right)}{4} + \left(\frac{2r_{\mathrm{i}\_t}}{d_{\mathrm{A\_0}}+\Delta d_{\mathrm{A}\_t}}-0.5\right)\left(d_{\mathrm{A\_0}}+\Delta d_{\mathrm{A}\_t}\right)\cos\alpha_{t} \quad (35)$$

The solution of simultaneous equations (34) and (35) by Newton- Raphson method can bring the δ_{Ar_t}, δ_{Aa_t} and θ_t calculation results based on the known X_{1j_t}, X_{2j_t}, δ_{Aij_t}, and δ_{Aoj_t} . Then X_{1j_t}, X_{2j_t}, δ_{ij_t}, δ_{oj_t} must be recalculated based on the known δ_{r_t},δ_{a_t} and θ_t values above. This cycle computing will not be terminated until the results of δ_{Ar_t}, δ_{Aa_t} and θ_t meet the calculation accuracy requirements.

After these solutions, thermal variations of relative ring radial, axial and angular displacements of angular contact ball bearing caused by its temperature rise T_{A_t}-T_0 can be ultimately calculated by:

$$\begin{cases} \overline{\delta_{\mathrm{A\_r}}}\Big|_{T_{\mathrm{A}\_t}-T_0} = \delta_{\mathrm{Ar}\_t} - \delta_{\mathrm{Ar}\_0} \\ \overline{\delta_{\mathrm{A\_a}}}\Big|_{T_{\mathrm{A}\_t}-T_0} = \delta_{\mathrm{Aa}\_t} - \delta_{\mathrm{Aa}\_0} \\ \overline{\theta_{\mathrm{A\_r}}}\Big|_{T_{\mathrm{A}\_t}-T_0} = \theta_t - \theta_0 \end{cases} \tag{36}$$

4 Thermal errors modeling method of motorized spindle unit

Based on thermal variation modeling of relative ring displacement of 2 typical spindle bearings in Section 3, this section analyzes the thermal error occurrence of the motorized spindle unit, and correspondingly introduces a comprehensive and transient modeling method for the spindle thermal errors. This method can be effectively used in the design phase of various motorized spindle units.

4.1 Occurrence of spindle thermal errors

As shown in Fig. 10, inside the physical structure of the applied motorized spindle unit, 4 angular contact ball bearings construct its spindle front bearing group, which has a double-DBB assembling method and the axial positioning preload. Meanwhile, the back bearing is a short cylindrical roller bearing, which allows the axial relative shift of its inner and outer ring. The spindle motor is placed between the front bearing group and the back bearing, and its rotor and the shaft are assembled with a press-fit method. The front bearing group, back bearing and the built-in motor (including stator and rotor) are main heat generating parts. When the motorized spindle unit is in operation, the generated heat from these heat generating parts will continuously raise their temperatures. Because the spindle shaft is directly connected with them, the shaft has a relative higher temperature rise owing to its heat transfer from the heat generating parts above. According to the thermo-elastic principle, the temperature rises of spindle front bearings, built-in motor, back bearing and shaft can cause their thermal deformations. Generally, these thermal deformations can contribute to spindle thermal errors (thermal displacement of spindle nose). They are spindle linear thermal error on axial/ radial directions and angular thermal errors. The former means the linear thermal displacement of spindle nose along X\Y\Z axis, and the latter means the angular thermal displacement of spindle nose around X\Y axis. According to the thermal analyses about motorized spindle unit, the reasons for spindle thermal errors (thermal displacements of spindle nose) can be approximately speculated as follows:

1) Spindle Z linear thermal error is ascribed to the shaft thermal elongation owing to its heat transfer from bearings.

Because the spindle shaft has the Z-axis symmetric structure, it has similar thermal deformations on its radial directions. Thus it can be speculated that only axial thermal elongation of spindle shaft can cause spindle axial thermal errors. Fortunately, the axial relative shift of inner and outer ring of spindle back bearing (short cylindrical roller bearing) can make the majority of spindle shaft has an axial backward movement when it is expended by structural heat transfer. This design can reduce the thermal contribution from spindle internal generated heat to spindle Z linear thermal error to some extent.

2) Spindle X\Y linear and angular thermal errors are attributed to the thermal variations of bearing relative ring displacements.

Because the parts of spindle bearings (such as the outer ring, inner ring and rollers) also have the Z-axis symmetric structures, their thermal deformations can hardly contribute directly to radial linear and angular thermal displacements of spindle nose. Thus it can be speculated that spindle Y/Z radial linear and angular thermal displacements can only be attributed to the thermal variations of bearing relative ring displacements, which are caused by the comprehensive effect of both the bearing external loads and temperature variations.

In this paper, these 2 assumptions above can lead to the development of the analytical simulation method to analyze thermal errors of the motorized spindle unit. Besides, they can clarify that heat generations of spindle front bearing group, back bearing and the built-in motor (including stator and rotor) are the root reason for the spindle thermal errors. Therefore, in order to promote the accuracy of motorized spindle unit, as revealed in Fig. 10, 3 helical coolant channels are designed nearby every spindle heat generating part, to allow flowing coolants to absorb their generating heat. This method can reduce thermal influences from heat generating parts onto spindle accuracy effectively.

4.2 Thermal errors modeling method of motorized spindle unit

With the modeling intention for spindle heat transfer - structural temperature rise - thermal errors, a comprehensive method based on the analytical modeling and FE simulation technology is described in Fig. 11. On one hand, in the numerical simulation process, the powers of spindle heat generating parts and the coefficient of convection heat transfer of ambient air/ flowing coolants are firstly modeled based on necessary spindle design and working condition parameters. Then based on these heat load/ boundary conditions, the heat - fluid - solid coupling FE simulations of motorized spindle unit are finished to provide the analytical calculation process with the bearing temperature, spindle Z thermal elongation and the time delay modification. On the other hand, the analytical calculation process firstly finishes the static balance analysis of spindle rotating unit based on the spindle structural design parameters and cutting loads, to determine the working loads onto every spindle bearing. Then based on the spindle temperature simulation results and these bearing loads, thermal variations of relative ring displacement of short cylindrical roller bearing and angular contact ball bearing are obtained by the method in Section 3. Eventually, the spindle X\Y linear and angular thermal errors are obtained based on these thermal variations, and their time delay modifications are finished according to the time delay between the occurrences of the steady spindle temperature distribution and the Z thermal elongation. The realization methods of the numerical simulation and analytical calculation process above are introduced in Section 4.2.1 and 4.2.2 respectively.

4.2.1 Numerical simulations for thermal errors modeling of motorized spindle unit

(1) Internal generating heat analysis

When the spindle unit is in rotational running state, the power loss of its motor and bearing friction heat are the foremost internal generating heat sources. Generally, these sources contribute greatly onto spindle temperature elevation and lead to thermal deformations of spindle parts, which cause ultimately its thermal errors. Based on experiences, the heat generating power of spindle motor Q_{Mo} is approximately 220W in this paper. Meanwhile, the friction heat power value of spindle bearings can be determined by the following method, and the expressions of the letters in this method can be found in the 'Nomenclature' section of this paper:

$$Q_{\mathrm{Fr/Ba}} = 1.047\times 10^{-4} n\left(M_0 + M_1\right) \tag{37}$$

In equation (37), M_0 brought by the viscosity of bearing lubricant and M_1 caused by the bearing applied force load can be respectively calculated as:

$$M_0 = \begin{cases} 10^{-7} f_0 (\nu_0 n)^{2/3} D_{\mathrm{m}}{}^3, \nu_0 n \geq 2000 \\ 160 \times 10^{-7} f_0 D_{\mathrm{m}}{}^3, \nu_0 n < 2000 \end{cases} \tag{38}$$

$$M_1 = f_1 F_\beta D_{\mathrm{m}} \tag{39}$$

(2) Heat transfer coefficient analysis

The rotating spindle parts exposed to ambient air (such as the test bar) make relative movement between spindle outer surfaces and ambient air. The coefficient of this forced convection heat transfer can be obtained by the following method. The letter meaning of these equations can be found in the ‘Nomenclature’ section of this paper as well:

$$h_{\mathrm{f}} = \frac{Nu\lambda}{l_{\mathrm{e}}} \tag{40}$$

In the equation (40) above:

$$\begin{cases} Nu = 0.133 \mathrm{Re}^{\frac{2}{3}} \mathrm{Pr}^{\frac{1}{3}} \\ \mathrm{Re} = \dfrac{u_{air} l_{\mathrm{e}}}{\nu_{air}} \\ l_{\mathrm{e}} = \dfrac{\sum_i^n d_{\mathrm{e}\_i} l_{\mathrm{e}\_i}}{\sum_i^n l_{\mathrm{e}\_i}} \\ u_{air} = \dfrac{\pi l_{\mathrm{e}}}{60} n \end{cases} \tag{41}$$

On the other hand, stationary surfaces of spindle structure mainly interact with ambient air by the natural convection and its heat transfer coefficient h_{n} =9.7 W/m^{2}K is provided by Reference [22].

(3) Heat - fluid - solid coupling FE simulations for motorized spindle unit

The heat powers of spindle heat generating parts (bearings and motor) and the coefficient of convective heat transfer from ambient air calculated above are used as the heat loads and thermal boundary conditions for transient heat-fluid-solid coupling FE simulations for spindle temperature and thermal deformation distributions. In ANSYS, the 3D CAE model of motorized spindle unit structure and its internal flowing coolants are established and meshed. To begin with, all the thermal contact resisters of joints in this spindle model are ignored except two critical ones: bearing housing - bearing outer ring (6.06e-4 m^2K/W) and bearing inner ring - spindle shaft (1.37e-4 m^2K/W). The determinations of these thermal contact resistance values for critical spindle joints were by experimental methods [23]. Secondly, the concerned fluid and solid material properties in Table 1 are assigned to their respective regions of the meshed spindle model. Thirdly, the spindle structure model being ignored, the meshed coolant models are tackled in Fig. 12: the coolant supply temperatures (25°C/20°C/15°C) and volume flow rates (5L/min) for front bearings, back bearing and motor are set up onto their inlet surfaces respectively; The outlet surfaces of them are exerted by 0 Pa pressure. The arrows in Fig. 12 point out the flowing directions of all the spindle coolants. Fourthly, as illustrated in Fig. 13, the 3D 0-displacement constraints are exerted onto the spindle structure. Meanwhile, in these spindle FE simulations, the heat powers of spindle motor and front/ back bearings (calculated based on the spindle working condition: 4000RPM rotation speed/ empty load) and 20℃ force/ natural ambient convection temperatures are adopted as the heat loads and thermal boundary conditions. After these preparations, the temperature and thermal deformation simulation results of motorized spindle unit are solved by ANSYS software and according to the heat - fluid - solid coupling model: The heat generation process and the fluid-solid conjugate heat transfer are obtained by solving the following energy equation [24]:

$$\frac{\partial}{\partial t}\left(\rho_{\text{oil\_sol}} H_{\text{en}}\right) + \nabla \bullet \left[\vec{v}\left(\rho_{\text{oil\_sol}} H_{\text{en}} + p\right)\right] = \nabla \bullet \left[k_{\text{oil\_sol}} \nabla T + \left(\overset{=}{\tau}\,\vec{v}\right)\right] + S_{\text{h}} \tag{42}$$

Meanwhile, with the assumption that spindle coolants are in the laminar and steady viscous incompressible flow regime, the coolant flow fields are simulated by solving the equation (43):

$$\begin{cases} \dfrac{\partial u}{\partial x} + \dfrac{\partial v}{\partial y} + \dfrac{\partial w}{\partial z} = 0 \\ \dfrac{\partial}{\partial t}\left(\rho_{\text{oil}}\,\vec{v}\right) + \nabla\left(\rho_{\text{oil}}\,\vec{v}\,\vec{v}\right) = -\nabla p + \nabla\left(\overset{=}{\tau}\right) \end{cases} \tag{43}$$

The letter meaning of equations (42) and (43) can be seen in the ‘Nomenclature’ section.

(4) Optimization corrections for spindle simulation parameters

Based on the modeling method of heat loads, thermal boundary conditions and the spindle FE simulation methods above, the temperature behavior simulation modeling for motorized spindle unit can be finished. Being the crucial preparation for modeling method of spindle thermal errors, the accuracy of spindle temperature simulation performs a perfectly vital influence onto the accuracy of spindle thermal error modeling. However, because the presented models of the heat loads, thermal boundary conditions above are mainly relied on traditional and empirical methods, they make spindle temperature simulation results so different with actual ones. Therefore, the satisfactory accuracy of the spindle simulated temperatures must be obtained by the optimization correction method about heat loads, thermal boundary condition parameters: To begin with, both of the heat generation powers and the heat transfer coefficients obtained by empirical method in Section 4.2.1 (1) and (2) are designed to be accurately corrected based on the following method:

$$\begin{cases} Q_{\mathrm{Fr/Mo/Ba}}' = k_{Q\_\mathrm{Fr/Mo/Ba}} \bullet Q_{\mathrm{Fr/Mo/Ba}} + b_{Q\_\mathrm{Fr/Mo/Ba}} \\ h_{\mathrm{f/n}}' = k_{h\_\mathrm{f/n}} \bullet h_{\mathrm{f/n}} + b_{h\_\mathrm{f/n}} \end{cases} \quad (44)$$

In equation (44) above, the proportionality coefficient *k* and deviation correction coefficient *b* are utilized to accurately correct heat generation power *Q* and the heat transfer coefficient *h*.

Besides, these correction coefficients above must be determined based on the optimization method. The vector of design variables for optimization is:

$$\boldsymbol{X} = [X_1, X_2, X_3, X_4, X_5, X_6, X_7, X_8, X_9, X_{10}]^{\mathrm{T}} = [k_{Q\_\mathrm{Fr}}, b_{Q\_\mathrm{Fr}}, k_{Q\_\mathrm{Mo}}, b_{Q\_\mathrm{Mo}}, k_{Q\_\mathrm{Ba}}, b_{Q\_\mathrm{Ba}}, k_{h\_\mathrm{f}}, b_{h\_\mathrm{f}}, k_{h\_\mathrm{n}}, b_{h\_\mathrm{n}}]^{\mathrm{T}} \quad (45)$$

Based on the initial values of these correction coefficients, the values of design variables are dynamically generated to correct heat load and thermal boundary condition parameters according to equation (44), then to be used for the circulation heat - fluid - solid coupling FE simulations to get spindle transient simulated temperatures $T_{\mathrm{Fr/Mo/Ba}}$. In order to get satisfactory agreements between the simulated temperatures $T_{\mathrm{Fr/Mo/Ba}}$ and the experimental data $\overline{\overline{T}}_{\mathrm{Fr/Mo/Ba}}$, the objective function of this optimization is:

$$\min f(\boldsymbol{X}) = \min \sqrt{\left(T_{\mathrm{Fr}} - \overline{\overline{T_{\mathrm{Fr}}}}\right)^2 + \left(T_{\mathrm{Mo}} - \overline{\overline{T_{\mathrm{Mo}}}}\right)^2 + \left(T_{\mathrm{Ba}} - \overline{\overline{T_{\mathrm{Ba}}}}\right)^2} \quad (46)$$

In equation (46), spindle experimental temperature values $\overline{\overline{T_{\mathrm{Fr/Mo/Ba}}}}$ must be obtained by the experimental method introduced in Section 5.1. Based on this optimization method, the accurate correction of heat loads and thermal boundary condition parameters for spindle FE simulations can be finished. Specially, in order to realize the general applicability of these parameter corrections, the optimization above must be repeated based on various spindle working conditions to determine the general correction coefficients.

(5) Numerical simulation results of motorized spindle unit

Based on the accurately corrected heat load and thermal boundary condition parameters and the heat - fluid - solid coupling FE simulation method for motorized spindle unit, spindle simulated thermal behaviors can be obtained. Fig. 14 shows the time-varying average temperatures of front bearing group and back bearing with 25℃/20℃/15℃ coolant supply temperature, which are obtained from spindle FE simulation results. It can be seen from Fig. 14 that, the all the bearing temperatures have the increasing tendencies with time, and the time - varying temperature of front bearing group is always higher than back bearing. The bearing temperatures with 25℃ and 20℃ coolant supply temperatures are higher than ambient temperature 20℃, and the former is higher than the latter. Besides, the bearing temperature with 15℃ coolant supply temperature is lower than ambient temperature. These transient simulated temperatures of spindle bearings are adopted into the thermal variation modeling of relative ring displacement of spindle bearings in Section 3, so as to finish the thermal errors modeling of motorized spindle unit. Meanwhile, there is a time delay between the occurrence of Z thermal displacement of spindle nose and the bearing temperature rise in spindle simulation results. Its scale can be the approximate guidance for the time modification onto Z linear thermal error modeling results of motorized spindle unit.

4.2.2 Analytical method for thermal errors modeling of motorized spindle unit

(1) Force balance analysis of spindle rotating unit

Based on the spindle temperature numerical simulation results, the static force balance condition of spindle rotating unit must be analyzed, in order to establish the analytical relationship between the thermal variations of relative ring displacement of spindle bearings and spindle thermal errors. As revealed in Fig. 15, the cutting load onto the working spindle nose can be decomposed into 3 force components F_X/ F_Y/ F_Z and 2 moment components M_X/ M_Y. Meanwhile, the spindle rotation unit bears the gravity G^{spi}, and there is the axial preload F_P onto the spindle front bearing group (angular contact ball bearings are numbered as 1-4). The concerned structural design parameters of motorized spindle unit in Fig. 15 are listed in Table 2.

Firstly, because the short cylindrical roller bearing (back bearing) cannot bear its axial load, and these 4 angular contact ball bearings are assembled by a double-DBB assembling method, the axial force onto every angular contact ball bearing can be related to force component F_Z onto spindle nose and the axial positioning preload F_P onto front bearing group:

$$\begin{cases} F_{A\_a(1)} = F_{A\_a(2)} = \dfrac{F_P}{2} + \dfrac{F_Z}{4} \\ F_{A\_a(3)} = F_{A\_a(4)} = \dfrac{F_P}{2} - \dfrac{F_Z}{4} \end{cases} \tag{47}$$

Secondly, the double-DBB assembling method can make the angular contact ball bearings have the following moment relationships in the Y-Z plane of Fig. 15:

$$\begin{cases} M_{A\_X(1)} = M_{A\_X(2)} \\ M_{A\_X(3)} = M_{A\_X(4)} \\ M_{A\_X(2)} = -M_{A\_X(3)} \end{cases} \tag{48}$$

Thirdly, in the Y-Z plane of Fig. 15, there is still the force balance relationship between the force component F_Y onto spindle nose, gravity and the radial loads of short cylindrical roller bearing and angular contact ball bearings:

$$\sum_{i=1}^{4} F_{A\_rY(i)} + F_{C\_rY} = F_Y + G^{spi} \tag{49}$$

Eventually, the moment balance of the spindle rotating unit in the Y-Z plane can be described as:

$$
\left\{
\begin{aligned}
&F_{\mathrm{Y}}\left(S+L_{1-2}+L_{2-3}+L_{3-4}+L\right)-G^{\mathrm{spi}}X_{\mathrm{G}}+M_{\mathrm{X}} \\
&=F_{\mathrm{A\_rY(1)}}S+F_{\mathrm{A\_rY(2)}}\left(S+L_{1-2}\right)+F_{\mathrm{A\_rY(3)}}\left(S+L_{1-2}+L_{2-3}\right)+F_{\mathrm{A\_rY(4)}}\left(S+L_{1-2}+L_{2-3}+L_{3-4}\right)+M_{\mathrm{A\_X(3)}}+M_{\mathrm{A\_X(4)}} \\
&-M_{\mathrm{A\_X(1)}}-M_{\mathrm{A\_X(2)}} \\
&F_{\mathrm{Y}}\left(L_{1-2}+L_{2-3}+L_{3-4}+L\right)+G^{\mathrm{spi}}\left(S-X_{\mathrm{G}}\right)+M_{\mathrm{X}} \\
&=F_{\mathrm{C\_rY}}S+F_{\mathrm{A\_rY(2)}}L_{1-2}+F_{\mathrm{A\_rY(3)}}\left(L_{1-2}+L_{2-3}\right)+F_{\mathrm{A\_rY(4)}}\left(L_{1-2}+L_{2-3}+L_{3-4}\right)+M_{\mathrm{A\_X(3)}}+M_{\mathrm{A\_X(4)}}-M_{\mathrm{A\_X(1)}}-M_{\mathrm{A\_X(2)}} \\
&F_{\mathrm{Y}}\left(L_{2-3}+L_{3-4}+L\right)+G^{\mathrm{spi}}\left(S-X_{\mathrm{G}}+L_{1-2}\right)+M_{\mathrm{X}} \\
&=F_{\mathrm{C\_rY}}\left(S+L_{1-2}\right)-F_{\mathrm{A\_rY(1)}}L_{1-2}+F_{\mathrm{A\_rY(3)}}L_{2-3}+F_{\mathrm{A\_rY(4)}}\left(L_{2-3}+L_{3-4}\right)+M_{\mathrm{A\_X(3)}}+M_{\mathrm{A\_X(4)}}-M_{\mathrm{A\_X(1)}}-M_{\mathrm{A\_X(2)}} \\
&F_{\mathrm{Y}}\left(L_{3-4}+L\right)+G^{\mathrm{spi}}\left(S-X_{\mathrm{G}}+L_{1-2}+L_{2-3}\right)+M_{\mathrm{X}} \\
&=F_{\mathrm{C\_rY}}\left(S+L_{1-2}+L_{2-3}\right)-F_{\mathrm{A\_rY(1)}}\left(L_{1-2}+L_{2-3}\right)-F_{\mathrm{A\_rY(2)}}L_{2-3}+F_{\mathrm{A\_rY(4)}}L_{3-4}+M_{\mathrm{A\_X(3)}}+M_{\mathrm{A\_X(4)}}-M_{\mathrm{A\_X(1)}}-M_{\mathrm{A\_X(2)}} \\
&F_{\mathrm{Y}}L+G^{\mathrm{spi}}\left(S-X_{\mathrm{G}}+L_{1-2}+L_{2-3}+L_{3-4}\right)+M_{\mathrm{X}} \\
&=F_{\mathrm{C\_rY}}\left(S+L_{1-2}+L_{2-3}+L_{3-4}\right)-F_{\mathrm{A\_rY(1)}}\left(L_{1-2}+L_{2-3}+L_{3-4}\right)-F_{\mathrm{A\_rY(2)}}\left(L_{2-3}+L_{3-4}\right)-F_{\mathrm{A\_rY(3)}}L_{3-4}+M_{\mathrm{A\_X(3)}} \\
&+M_{\mathrm{A\_X(4)}}-M_{\mathrm{A\_X(1)}}-M_{\mathrm{A\_X(2)}}
\end{aligned}
\right.
\tag{50}
$$

To sum up, simultaneous equations (47) to (50) can be solved to get the radial force load $F_{\mathrm{C\_rY}}$ onto short cylindrical roller bearing and axial force load $F_{\mathrm{A\_aY}(i)}$ / radial force load $F_{\mathrm{A\_rY}(i)}$ / moment load $M_{\mathrm{A\_X}(i)}$ onto every angular contact ball bearing $(i=1,2,3,4)$ in the Y-Z plane. By the same method, those bearing loads in X-Z plane of Fig. 15 can be obtained as well.

(2) Applications for thermal variation modeling of relative ring displacements of spindle bearings

Based on the obtained axial force load $F_{\mathrm{A\_a}(i)}$, radial force load $F_{\mathrm{A\_rX}(i)}/F_{\mathrm{A\_rY}(i)}$, moment load $M_{\mathrm{A\_X}(i)}/M_{\mathrm{A\_Y}(i)}$ $(i=1,2,3,4)$ onto angular contact ball bearing and radial force load $F_{\mathrm{C\_rX}}/F_{\mathrm{C\_rY}}$ onto short cylindrical roller bearing, thermal variation calculations of relative ring displacements of these two kinds of spindle bearing can be gained by the modeling method introduced in Section 3. With the spindle shaft curve being ignored, the thermal variation of angular relative ring displacement of front bearing group is approximately equal to angular contact ball bearing 1/2 and opposite to angular contact ball bearing 3/4. Besides, the bearing temperature rises, which are required by this modeling method, must be obtained according to the heat - fluid - solid coupling FE simulation results of motorized spindle unit. The values of concerned design parameters of 2 kinds of spindle bearing are listed in Table 3.

(3) Modeling of thermal variations of bearing relative ring displacements - spindle thermal errors

Based on the obtained thermal variations of radial relative ring displacement of short cylindrical roller bearing and angular contact ball bearing, spindle X\Y linear and angular thermal errors can be gained according to the geometrical relationships in Fig. 16:

$$\begin{cases} \overline{\delta_{X}} = \left(1+\dfrac{L_{g}}{S_{g}}\right)\overline{\delta_{A\_rX(g)}} + \dfrac{L_{g}}{S_{g}}\overline{\delta_{C\_rX}} \\ \overline{\delta_{Y}} = \left(1+\dfrac{L_{g}}{S_{g}}\right)\overline{\delta_{A\_rY(g)}} + \dfrac{L_{g}}{S_{g}}\overline{\delta_{C\_rY}} \end{cases} \tag{51}$$

$$\begin{cases} \overline{\varepsilon_{X}} = \overline{\theta_{A\_rX(g)}} \\ \overline{\varepsilon_{Y}} = \overline{\theta_{A\_rY(g)}} \end{cases} \tag{52}$$

(4) Analytical results for thermal errors of motorized spindle unit

Fig. 17 shows the comparisons of analytical results for steady thermal errors of motorized spindle unit caused by three different coolant supply temperatures respectively. It can be seen from the comparisons that, 20℃ coolant supply temperature can cause the smaller linear and angular spindle thermal error ($\overline{\delta_{Y}}$=-18.9μm, $\overline{\delta_{Z}}$=58.2μm; $\overline{\varepsilon_{X}}$=-2.4e-005rad) than the other 2 conditions. Because there is 0 bearing loads in X-Z plane of Fig. 15, the values of $\overline{\delta_{X}}$ and $\overline{\varepsilon_{Y}}$ are analytically 0 in 3 conditions. It can be concluded from relationship between Figs. 14 and 17 that the scales of spindle thermal errors are closely associated with the bearing temperature rise scales: Both the thermal variations of relative ring displacements of spindle bearings and the heat transfer from spindle bearings to shaft can be ascribed to the spindle bearing temperature rises, thus the nearer to the ambient temperature the spindle bearing temperatures are, the smaller the spindle X\Y\Z linear thermal errors and X\Y angular thermal errors are. Furthermore, because the bearing temperature rises can be influenced by the modifications onto bearing coolant supply temperatures, the spindle thermal errors can be theoretically reduced by a reasonable regulation onto bearing coolant supply temperatures during the spindle operation.

5 Experimental verifications for spindle thermal errors modeling

In this section, the reliability of the presented thermal error modeling method of motorized spindle unit is verified by experimental methods. These verifications includes the simulated temperature and thermal errors comparisons, and done based on 25℃/20℃/15℃ coolant supply temperature respectively.

5.1 Experimental setup and schematization

As illustrated in Fig. 18, the temperatures and thermal errors of motorized spindle unit were measured by RTD sensors and eddy current displacement sensors respectively in the spindle experimental operation. On one hand, RTD sensors are located nearby spindle heat generating parts: T_A and T_B are measured to be the temperature of front bearings; T_C-T_F stand for the motor temperature; T_G and T_H are used for detecting the back bearing temperature. On the other hand, spindle thermal errors are detected by eddy current displacement sensors by using the inspection bar, the location of eddy current displacement sensors must be according to the standard method of spindle thermal errors [25]. When the motorized spindle unit was working at a 4000RPM rotating velocity in a consistent 20±0.2℃ temperature environment, its temperatures and thermal errors were continuously measured respectively by sensors above. Then the signals obtained from those two kinds of sensors were conveyed by signal acquisition system to the host computer. Experiments were done based on 5L/min supply volume flow rates and 25℃/20℃/15℃ supply temperatures of spindle coolants, to verify comprehensively the thermal modeling method of motorized spindle unit. The measurements in every condition would not be terminated until the changing scales of its signals in last hour were less than 15% of the ones in first hour [25].

5.2 Experimental results and analyses

According to the sensor locations in Fig. 18, the experimental temperature values of the heat generating parts of motorized spindle unit can be obtained based on the average values of the detections from RTD sensors T_A / T_B, T_C-T_F and T_G / T_H respectively, and the linear thermal errors $\overline{\delta_X} / \overline{\delta_Y} / \overline{\delta_Z}$ and the angular thermal errors $\overline{\varepsilon_X} / \overline{\varepsilon_Y}$ of motorized spindle unit can be calculated based on detected values from eddy current displacement sensors X(A)/Y(A)/X(B)/Y(B) according to the geometry relationship revealed in Fig. 18. These experimental data are used to be compared with the corresponding spindle thermal characteristics obtained by the modeling method in Section 4, which are revealed in Figs. 19 and 20 respectively.

On one hand, for spindle bearing temperatures, Fig. 19 shows that they increase with time in initial period, and gradually saturate to final temperatures when their heat generations balance with their heat dissipations. On the other hand, for spindle thermal errors, Fig. 20 illustrates that they also have the increasing tendencies, and the Z-linear (axial direction) thermal error has the greater disturbing effect onto machining accuracy than the other spindle thermal errors. It can be clarified in Figs. 19 and 20 that, modeled spindle temperatures and thermal errors are in good agreements with their experimental data in the condition of 20℃ coolant supply temperature. Their deviations can be analytically attributed to the inaccuracies of some modeling prerequisites, such as the spindle structural physical properties, heat loads and boundary conditions.

These agreements can also be obtained in the comparisons of the other 2 conditions, whose descriptions have been simplified for the limit of the paper. The consistencies can verify not only the reliability of the introduced thermal errors modeling method of motorized spindle unit, but also the correctness of the assumption that spindle linear thermal error on axial direction is mainly ascribed to shaft thermal elongation for its heat transfer from bearings, and spindle linear thermal errors on radial directions and angular thermal errors are mainly attributed to thermal variations of bearing relative ring displacements.

6 Conclusions

An analytical modeling method, based on the heat - fluid - solid coupling FE simulation, for a motorized spindle unit is presented in this paper, so as to predict the spindle thermal characteristics and study the occurrence mechanism of spindle thermal errors. This method is established with an emphasis on the analytical relationship between the thermal variations of spindle bearing relative ring displacements and the spindle linear thermal errors on radial directions/ angular thermal errors.

Specially, the thermal variation modeling of relative ring displacements of short cylindrical roller bearing and angular contact ball bearing can be guided theoretically by the thermal - mechanical models of rotating ring geometry and interference assembled rotating ring geometries. Core conclusions of the study as a whole are as follows:

(1) In the design and development phase of motorized spindle unit, the presented analytical modeling method for spindle thermal errors, based on the heat - fluid - solid coupling FE simulation, is reliable and accurate to predict and analyze spindle thermal characteristics, such as the temperature and thermal errors, which is verified by the comparison experiments.

(2) The verified reliability of the presented thermal errors modeling method of motorized spindle unit can clarify the correctness and reasonability of its prerequisites: Thermal variations of relative ring displacements of spindle bearings are dominant factors for the occurrence of spindle linear thermal errors on radial directions and angular thermal errors, and the thermal elongation of spindle shaft owing to the heat transfer from spindle bearings is the main reason for spindle thermal error on axial direction.

(3) Both the thermal variations of relative ring displacements of spindle bearings and the heat transfer from spindle bearings to shaft can be ascribed to the spindle bearing temperature rises. These temperature rises can be influenced by the modifications onto bearing coolant supply temperatures. Therefore, the spindle thermal errors can be theoretically reduced by a reasonable regulation onto bearing coolant supply temperatures, during the spindle operation.

Study prospects: Based on thermal characteristics analyses of motorized spindle unit in this paper, investigations about an appropriate and reasonable regulating strategy onto bearing coolant supply temperatures during the spindle operation will be emphasized in future studies. Its aim is to realize the stabilization of spindle temperatures and the decrease of spindle thermal errors.

Acknowledgment

All the authors acknowledge the state S & T projects for upmarket NC machine and fundamental manufacturing equipment of China (no. 2013ZX04005-013, no. 2014ZX04014-011, and no. 2015ZX04005001, resp.).

References

[1] K.L.H. Al-Shareeef, J.A. Brandon, On the effects of variations in the design parameters on the dynamic performance of machine tool spindle bearing system, Int. J. Mach. Tools Manuf. 30 (3) (1990) 431-445.

[2] L. Yang, W. H. Zhao, S. H. Lan, et al., A review on spindle thermal error compensation in machine tools, Int. J. Mach. Tools Manuf. 95 (2015) 20-38.

[3] H.J. Pahk, S.W. Lee, Thermal error measurement and real time compensation system for the CNC machine tools incorporating the spindle thermal error and the feed axis thermal error, Int. J. Mach. Tools Manuf. 20 (7) (2002) 487-494.

[4] T.J. Ko, T.W. Gim, J.Y. Ha. Particular behavior of spindle thermal deformation by thermal bending, Int. J. Mach. Tools Manuf. 43 (1) (2003) 17-23.

[5] J.S. Chen, W.Y. Hsu, Characterizations and models for the thermal growth of a motorized high speed spindle, Int. J. Mach. Tools Manuf. 43 (11) (2003) 1163-1170.

[6] C. Brecher, P. Hirsch, M. Weck, Compensation of thermo-elastic machine tool deformation based on control internal data, CIRP Ann. - Manuf. Technol. 53 (1) (2004) 299-304.

[7] Y. Kang, C.W. Chang, Y. Huang, et al., Modification of a neural network utilizing hybrid filters for the compensation of thermal deformation in machine tools, Int. J. Mach. Tools Manuf. 47 (2) (2007) 367-387.

[8] E. Gomez-Acedo, A. Olarra, J. Orive, et al., Methodology for the design of a thermal distortion compensation for large machine tools based in state-space representation with Kalman filter, Int. J. Mach. Tools Manuf. 75 (12) (2013) 100-108.

[9] E. Bitar-Nehme, J. R. R. Mayer, Thermal volumetric effects under axes cycling using an invar R-test device and reference length, Int. J. Mach. Tools Manuf. 105 (2016) 14-22.

[10] K. Liu, M. J. Sun, T. J. Zhu, et al., Modeling and compensation for spindle's radial thermal drift error on a vertical machining center, Int. J. Mach. Tools Manuf. 105 (2016) 58-67.

[11] H.T. Zhao, J.G. Yang, J.H. Shen, et al., Simulation of thermal behaviors of a CNC tool spindle, Int. J. Mach. Tools Manuf. 47 (6) (2007) 1003-1010.

[12] E. Creighton, A. Honegger, A. Tulsian, et al., Analysis of thermal errors in a high-speed micro-milling spindle, Int. J. Mach. Tools Manuf. 50 (4) (2010) 386-393.

[13] T. Holkup, H. Cao, P. Kolar, et al., Thermo-mechanical model of spindles, CIRP Ann. - Manuf.

Technol. 59 (1) (2010) 365-368.

[14]D.X. Li, P.F. Feng, J.F. Zhang, et al., Calculation method of convective heat transfer coefficients for thermal simulation of a spindle system based on RBF neural network, Int. J. Adv. Manuf. Technol. 70 (5) (2014) 1445-1454.

[15]S. Y. Jiang, H. B. Mao, Investigation of variable optimum preload for a machine tool spindle, Int. J. Mach. Tools Manuf. 50 (1) (2010) 19-28.

[16]D.J. Chen, M. Bonis, F.H. Zhang, et al., Thermal error of a hydrostatic spindle, Precis Eng. 35 (3) (2010) 512-520.

[17]E. L. Zheng, F. Jia, S. H. Zhu, Thermal modeling and characteristics analysis of high speed press system, Int. J. Mach. Tools Manuf. 85 (7) (2014) 87-99.

[18]J. Lee, D.H. Kim, C.M. Lee, A study on the thermal characteristics and experiments of high-speed spindle for machine tools, International Journal of Precision Engineering and Manufacturing. 16 (2) (2015) 293-299.

[19]C. Ma, J. Yang, L. Zhao, et al., Simulation and experimental study on the thermally induced deformations of high-speed spindle system, Appl Therm Eng. 86 (2015) 251-268.

[20]J.M. Gere, S.P. Timoshenko, Mechanics of materials: Second SI Edition, Van Nostrand Reinhold, New York, 1984.

[21]T.A. Harris, Rolling Bearing Analysis, Wiley, New York, 1984.

[22]M. Xu, S.Y. Jiang, Y. Cai, An improved thermal model for machine tool bearings, Int. J. Mach. Tools Manuf. 47 (1) (2007) 53-62.

[23]H.L. Zhao, Y.M. Huang, J.L. Xu, et al., Experiment research on thermal contact resistance of normal used joints, Journal of Xi'an University of Technology. 15 (3) (1999) 26-29.

[24]J.D. Anderson, Computational fluid dynamics: the basics with applications, McGraw Hill, New York, 1995.

[25]ISO 230-3-2007. Test code for machine tools - Part 3: Determination of thermal effects (Second Edition).

Table

Table 1 Material parameters in FE simulation for motorized spindle unit

	Spindle structure (45#)	Bearings (GCr15)	Rotor (copper)	Coolants (oil)
Density (kg/m^3)	7850	7830	8930	910
Thermal conductivity (w/(m·K))	70	40	398	0.13
Specific heat (J/(kg·K))	448	670	386	2090
Young's Modulus (GPa)	207	207	128	—
Poisson's ratio	0.254	0.3	0.34	—
Linear expansion coefficient (K^{-1})	1.18e-5	1.16e-5	1.22e-5	—

Table 2 Structural design parameters of motorized spindle unit

Design parameters	Scales
Distance between bearing 1 and 2/ 2 and 3/ 3 and 4 L_{1-2}/ L_{2-3}/ L_{3-4}	0.024m/ 0.048m/ 0.024m
Axial preload for spindle front bearing group F_P	780N
Distance between front bearing 4 and spindle nose L	0.13m
Distance between back bearing and front bearing 1 S	0.472m
Distance between back bearing and gravity center of spindle rotating unit X_G	0.27m
Gravity of spindle rotating unit G^{spi}	395N

Table 3 Design parameters of spindle bearings

Design parameters	Scales
Initial Interference fit value of bearing housing/ spindle - short cylindrical roller bearing $I_{\mathrm{CO\_0}} / I_{\mathrm{CI\_0}}$	2μm/ 6μm
Outer diameter Ⅰ/ Ⅱ/ Ⅲ of short cylindrical roller bearing $D_{\mathrm{CO}}^{\mathrm{I}}$ / $D_{\mathrm{CO}}^{\mathrm{II}}$ / $D_{\mathrm{CO}}^{\mathrm{III}}$	90mm/ 100mm/ 120mm
Inner diameter Ⅰ/ Ⅱ/ Ⅲ of short cylindrical roller bearing $D_{\mathrm{CI}}^{\mathrm{I}}$ / $D_{\mathrm{CI}}^{\mathrm{II}}$ / $D_{\mathrm{CI}}^{\mathrm{III}}$	48mm/ 65mm/ 74mm
Pitch diameter of short cylindrical roller bearing d_{m}	82mm
Roller number of short cylindrical roller bearing Z	13
Initial cross section length/ diameter of roller of short cylindrical roller bearing $d_{\mathrm{C\_0}} / l_0$	8mm/10mm
Diametric clearance of short cylindrical roller bearing P_{dC}	20μm
Initial interference fit value of bearing housing/ spindle - angular contact ball bearing $I_{\mathrm{AO\_0}} / I_{\mathrm{AI\_0}}$	2μm/ 6μm
Thermal contact resistance value of bearing housing/ spindle - short cylindrical roller bearing $R_{\mathrm{AO}} / R_{\mathrm{AI}}$	6.06e-4 m^2K/W/ 1.37e-4 m^2K/W
Outer diameter Ⅰ_1/ 2/ 3 of angular contact ball bearing $D_{\mathrm{AO}}^{\mathrm{I\_1}}$ / $D_{\mathrm{AO}}^{\mathrm{I\_2}}$ / $D_{\mathrm{AO}}^{\mathrm{I\_3}}$	130mm/ 132.541mm/ 133mm
Outer diameter Ⅱ/ Ⅲ of angular contact ball bearing $D_{\mathrm{AO}}^{\mathrm{II}}$ / $D_{\mathrm{AO}}^{\mathrm{III}}$	150mm/ 178mm
Inner diameter Ⅰ/ Ⅱ of angular contact ball bearing $D_{\mathrm{AI}}^{\mathrm{I}}$ / $D_{\mathrm{AI}}^{\mathrm{II}}$	42mm/ 100mm
Inner diameter Ⅲ_1'/ 2'/ 3' of angular contact ball bearing $D_{\mathrm{AI}}^{\mathrm{III\_1}}$ / $D_{\mathrm{AI}}^{\mathrm{III\_2}}$ / $D_{\mathrm{AI}}^{\mathrm{III\_3}}$	113mm/ 115.816mm/ 116mm
Length of outer/ inner grooves of angular contact ball bearing l_{o} / l_{i}	5.067mm/ 7.049mm
Initial contact angle of angular contact ball bearing α	25°
Radial clearance of angular contact ball bearing P_{dA}	20μm
Pitch diameter of angular contact ball bearing d_{m}	123mm
Roller number of angular contact ball bearing Z	20
Initial cross section diameter of roller of angular contact ball bearing $d_{\mathrm{A\_0}}$	10mm

***Highlights (for review)**

1 Thermal variations of relative ring displacements of spindle bearings are modeled.

2 Spindle thermal errors are analyzed to be closely related to the bearing thermal characteristics.

3 An analytical modeling method for spindle thermal errors is presented.

Figure

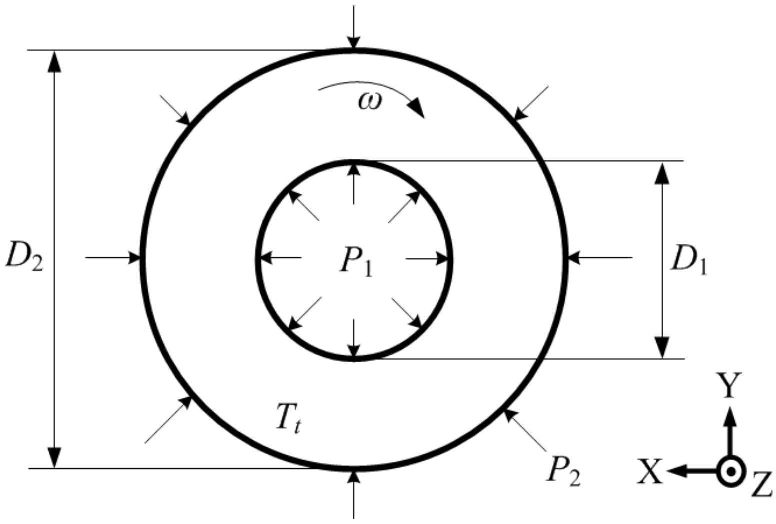

Fig. 1. Thermo-mechanical modeling of rotating ring geometry

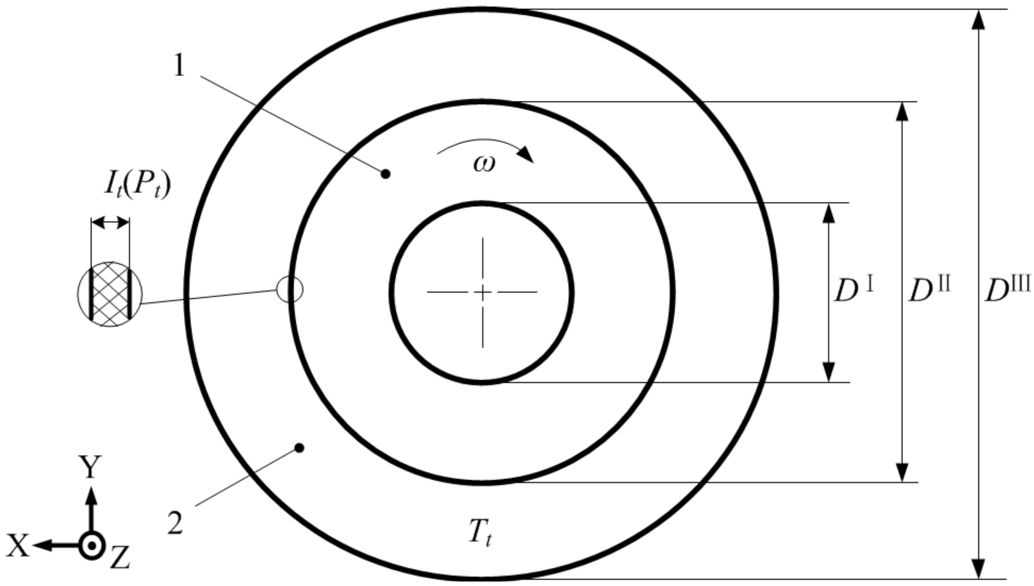

Fig. 2. Thermo-mechanical modeling of the interference assembled rotating ring geometries

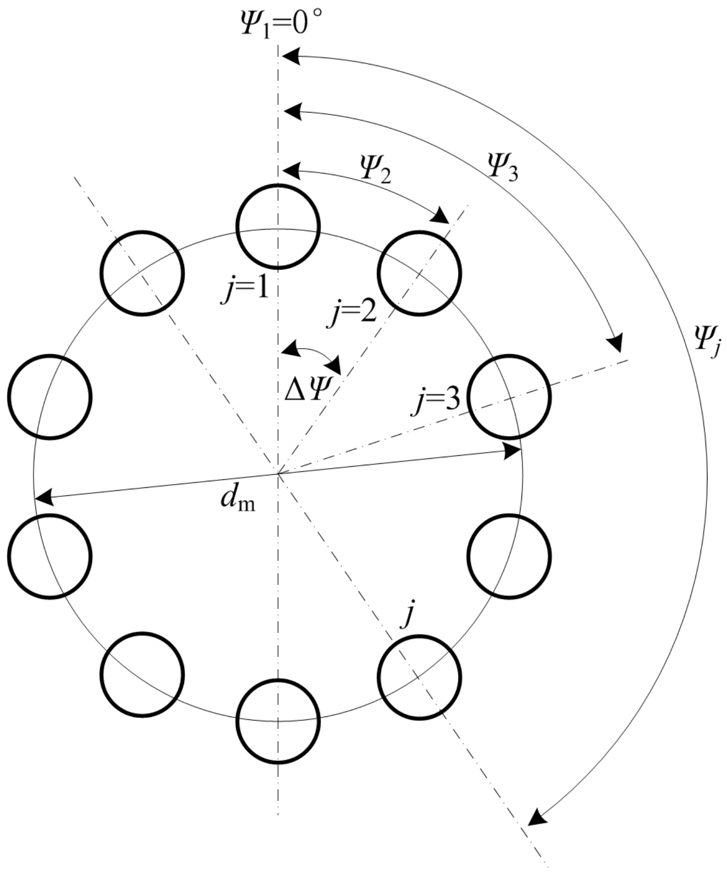

Fig. 3. Roller angular locations of typical bearings applied into motorized spindle unit

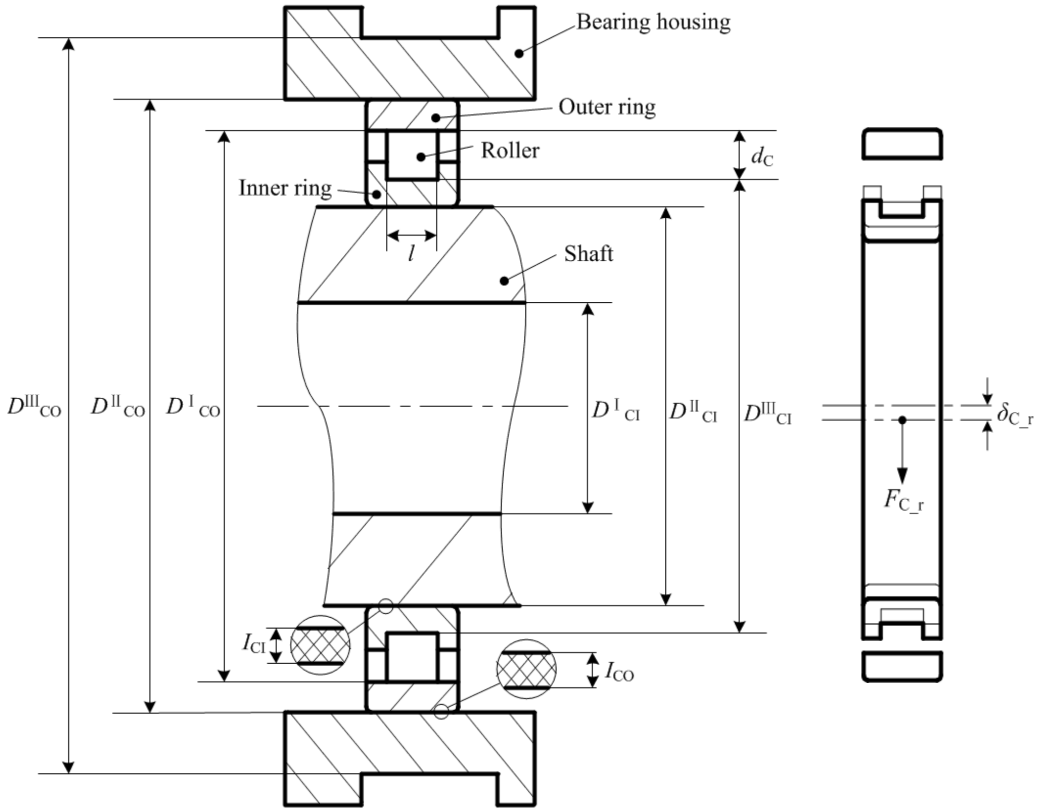

(a) Design scales

(b) Load and displacement

Fig. 4. Design scales of short cylindrical roller bearing and its load leading to displacement

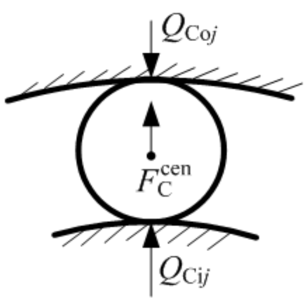

Fig. 5. Force analysis of the roller at angular location Ψ_j

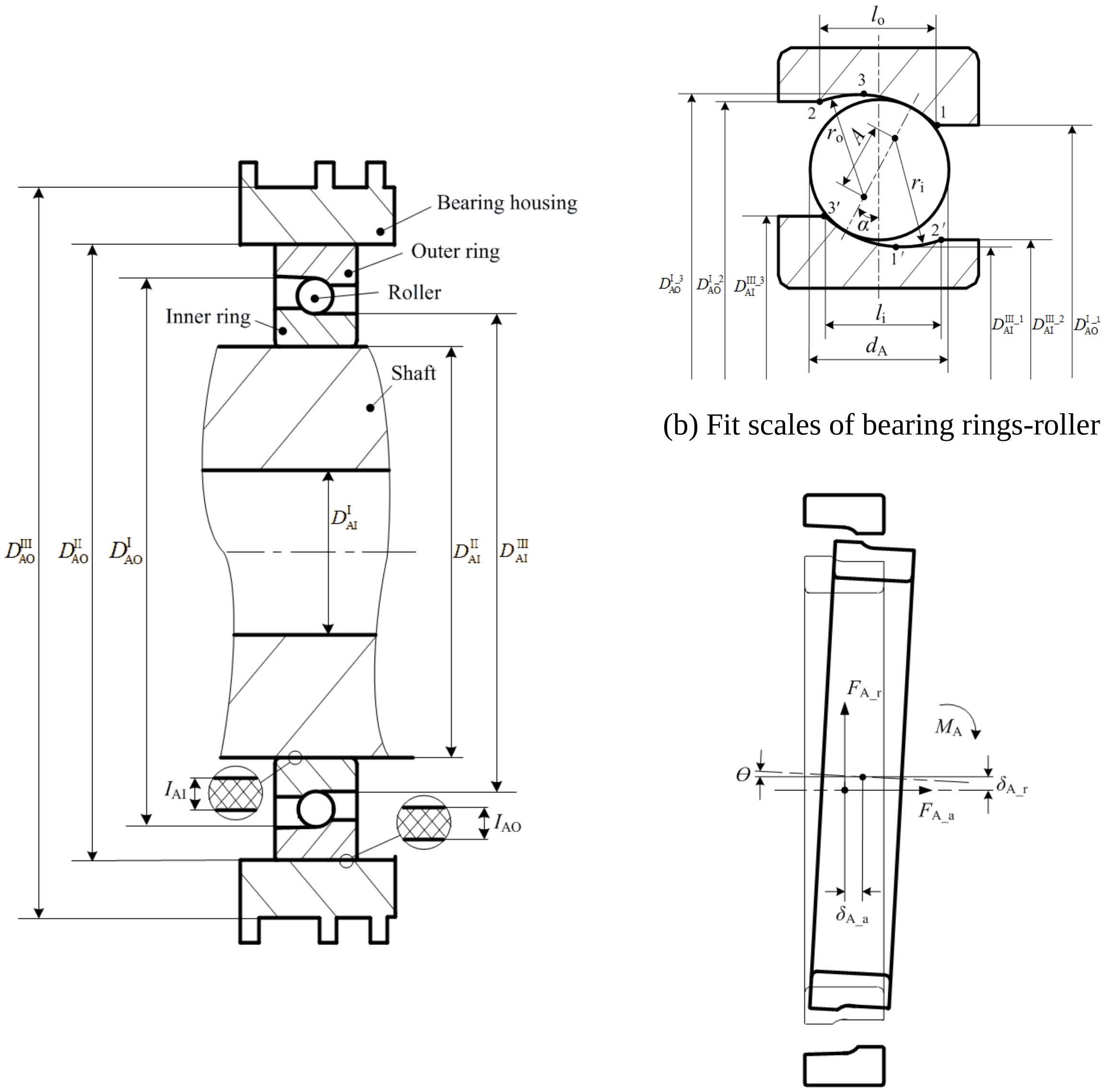

(b) Fit scales of bearing rings-roller

(a) Design scales

(c) Loads and displacements

Fig. 6. Design scales of angular contact ball bearing and its load leading to displacements

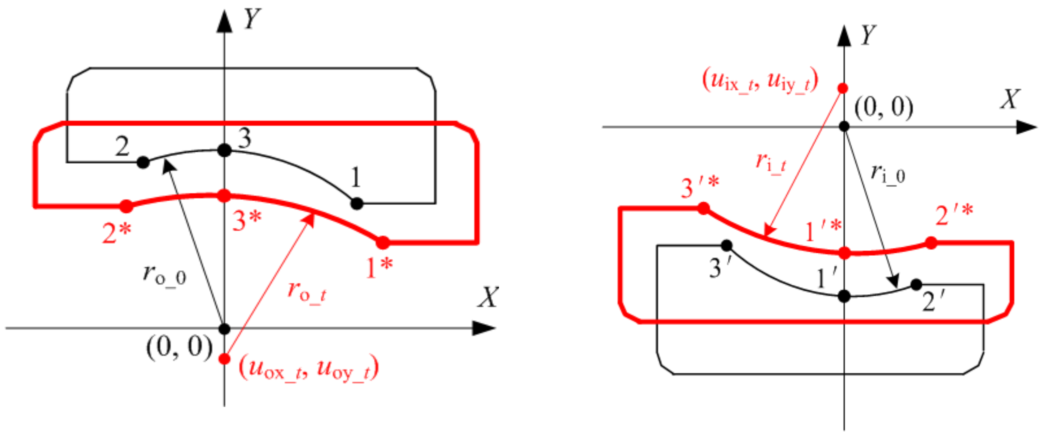

(a) Outer groove (b) Inner groove

Fig. 7. Thermal deformations of inner and outer grooves of angular contact ball bearing

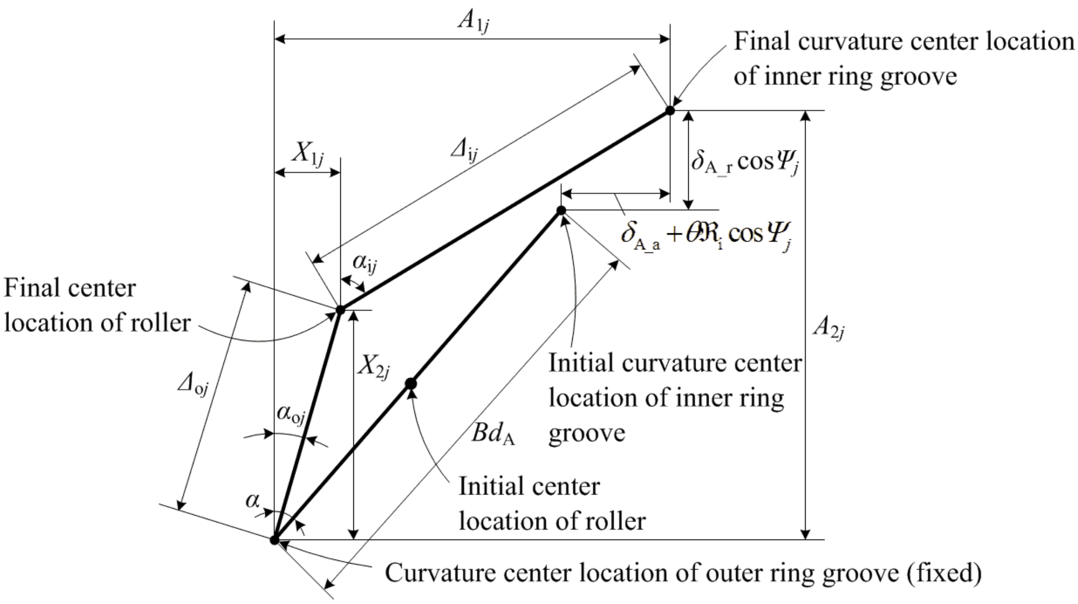

Fig. 8. Center locations of j^{th} ball roller and its corresponding inner and outer ring grooves of angular contact ball bearing (before and after external loads)

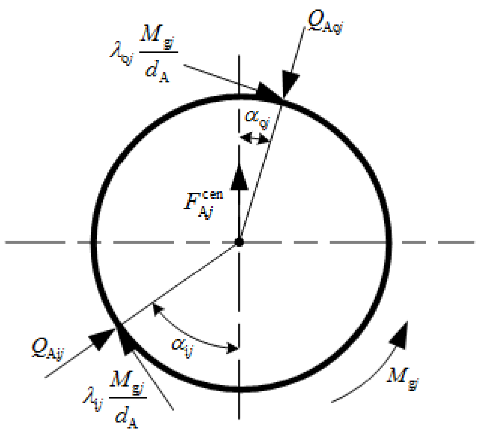

Fig. 9. Force-loads of j^{th} ball roller of angular contact ball bearing

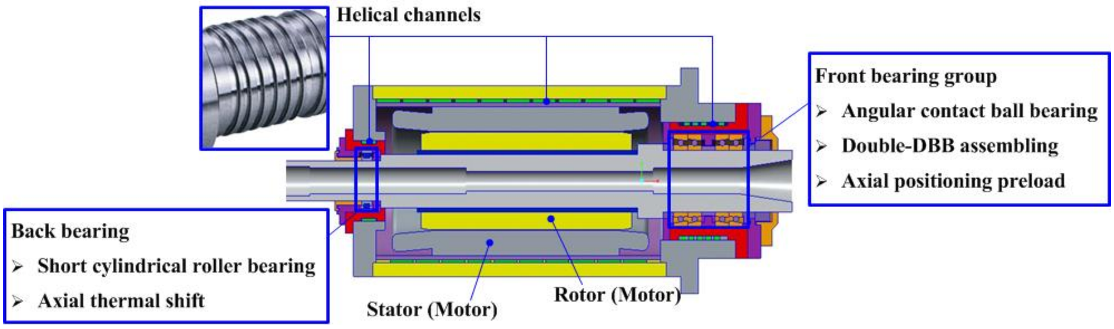

Fig. 10. Structure of motorized spindle unit

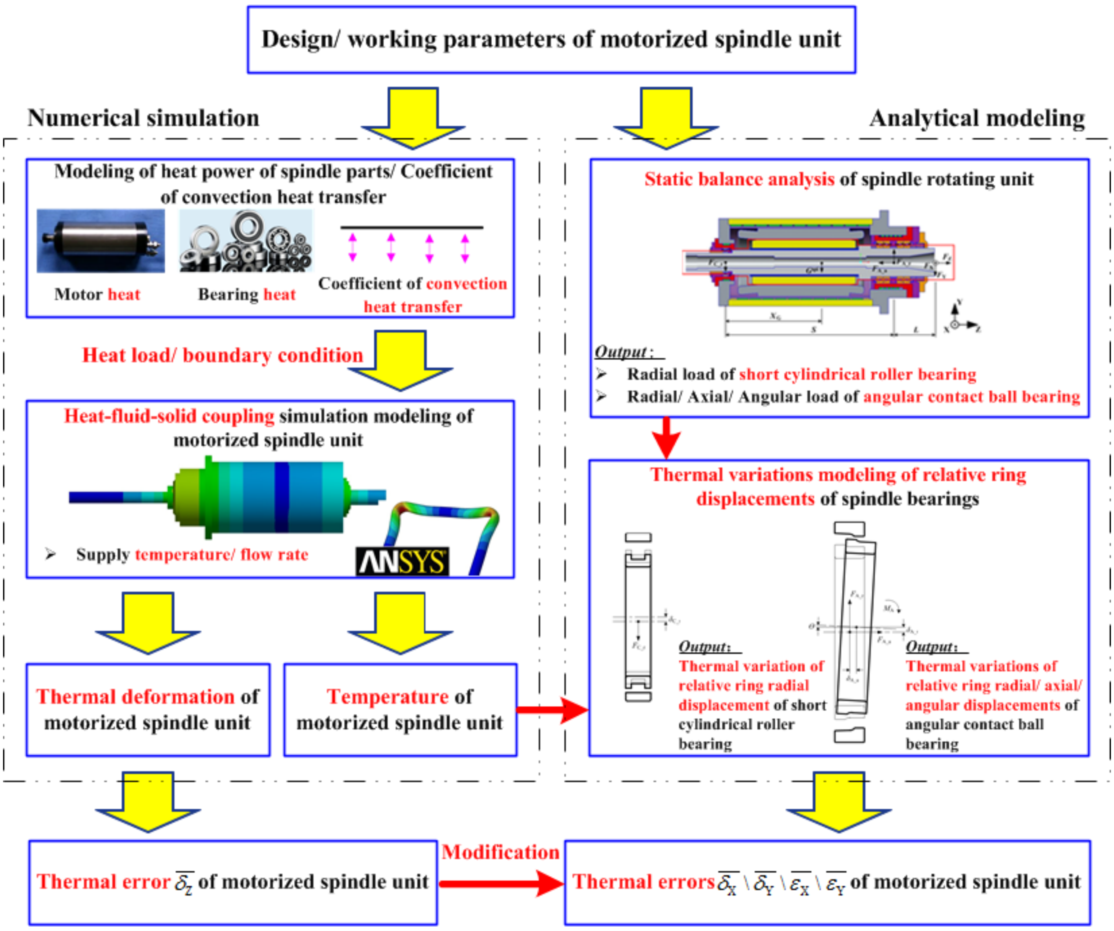

Fig. 11. Thermal error modeling method of motorized spindle unit

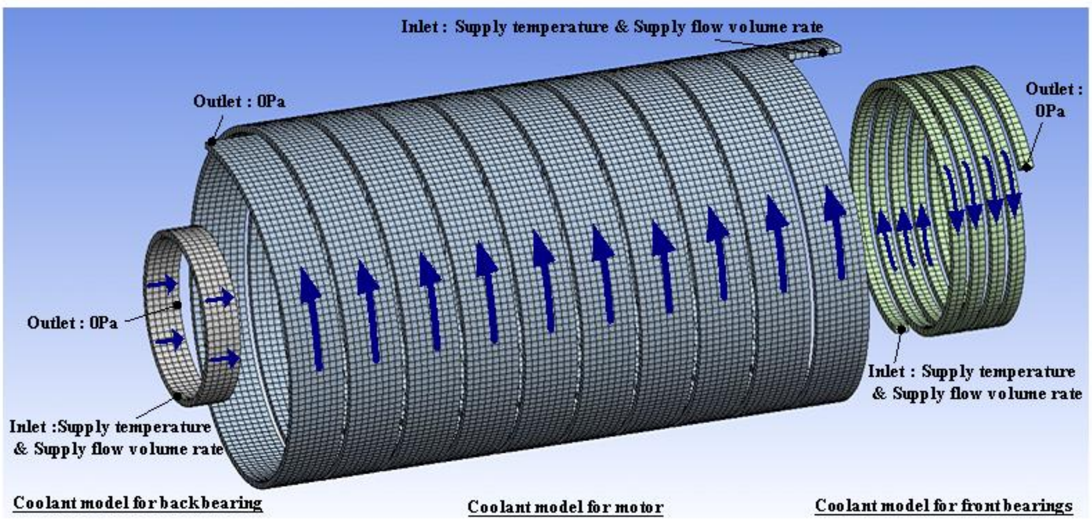

Fig. 12. Meshed flowing coolant CAE models and thermal boundary conditions

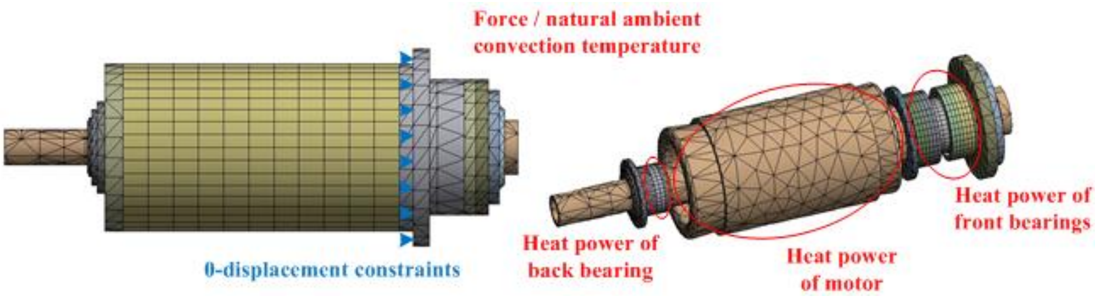

Fig. 13. Heat loads and thermal boundary conditions for spindle structure CAE model

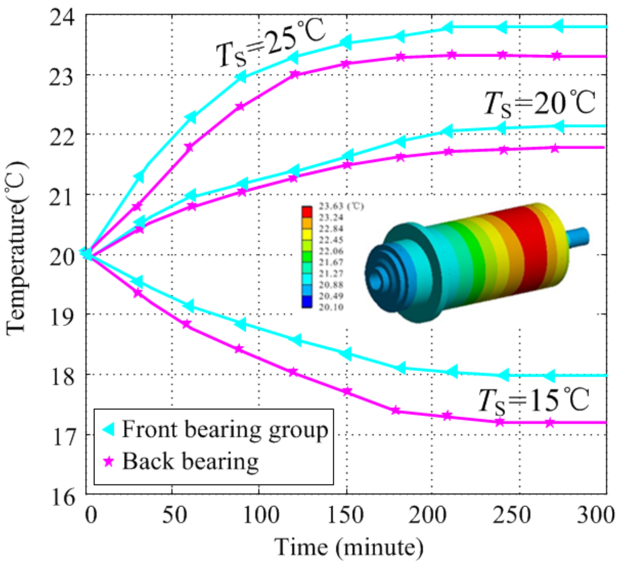

Fig. 14. Temperature simulation results of front bearing group and back bearing of motorized spindle unit

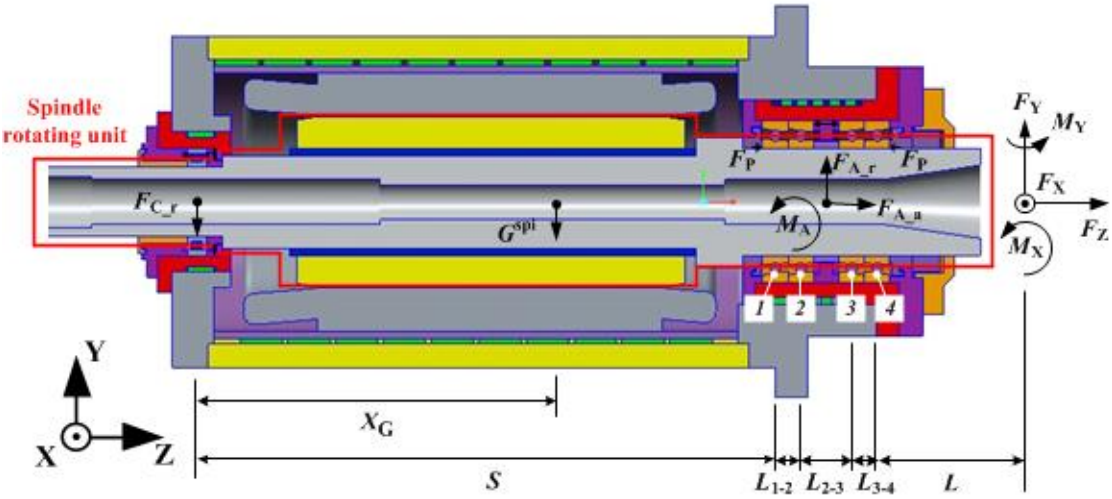

Fig. 15. Force balance analysis of spindle rotating unit

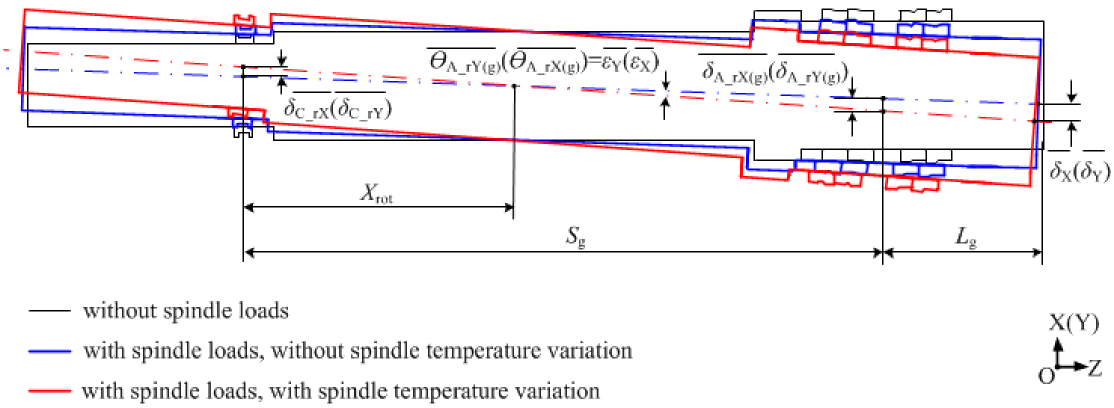

Fig. 16. Geometrical relationship between spindle thermal errors and thermal variations of relative ring displacement of spindle bearings

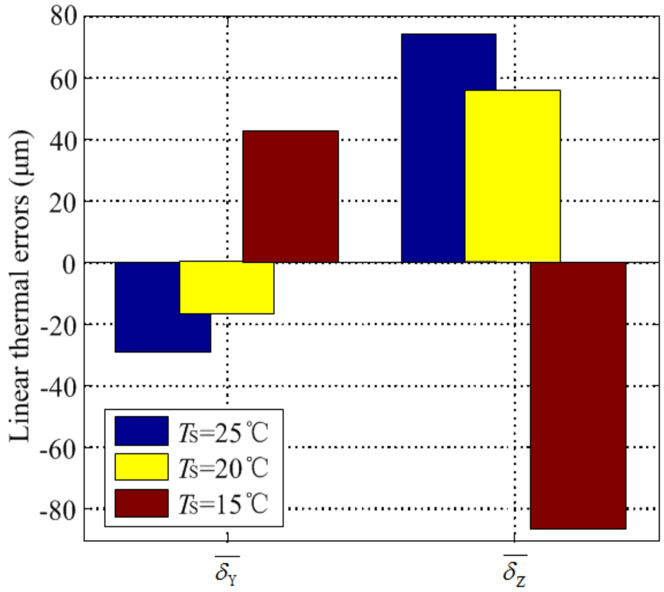

(a) Linear thermal errors

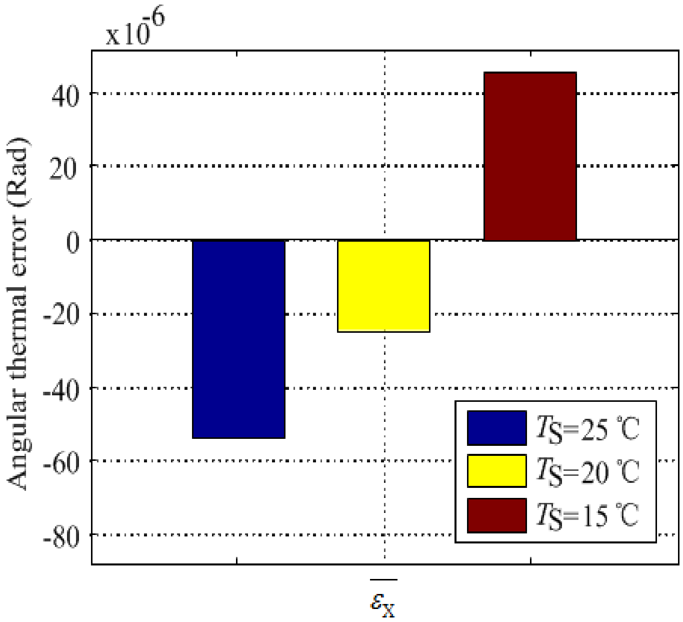

(b) Angular thermal error

Fig. 17. Analytical thermal error results of motorized spindle unit

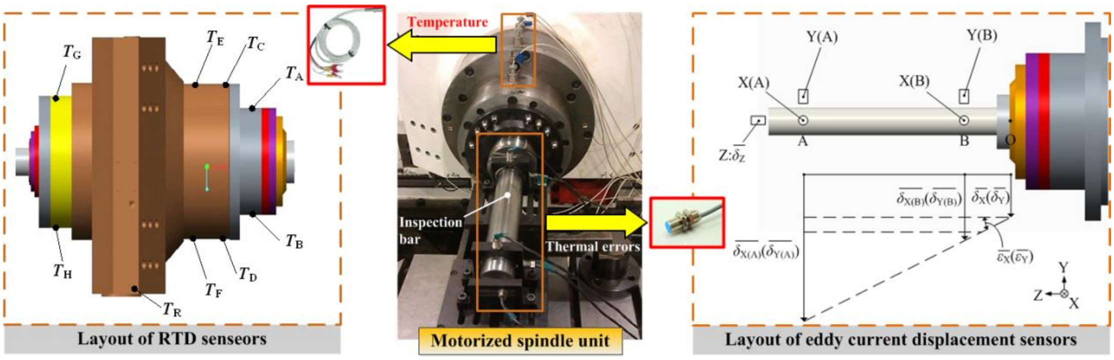

Fig. 18. Experimental setup

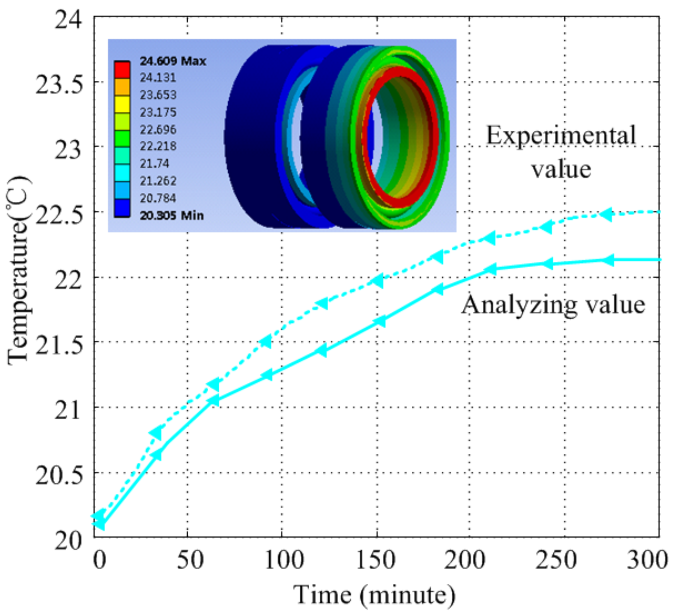

(a) Front bearing group

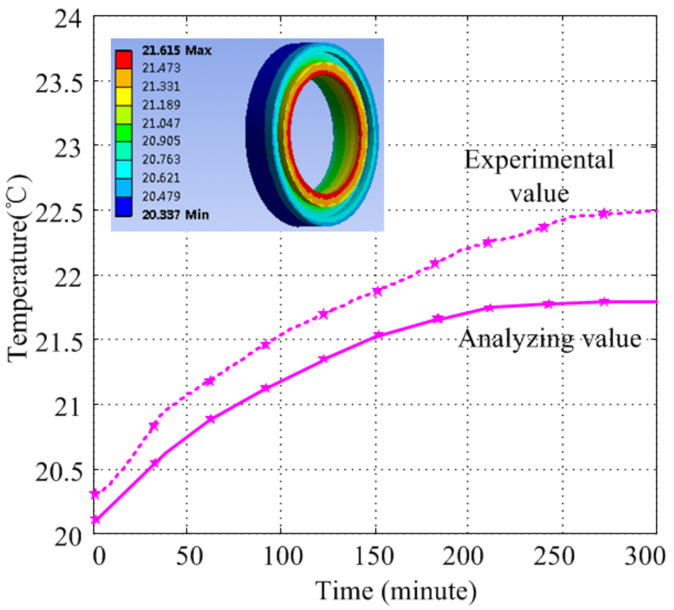

(b) Back bearing

Fig. 19. Spindle bearing temperature comparisons between experimental data and modeling results (T_S=20℃)

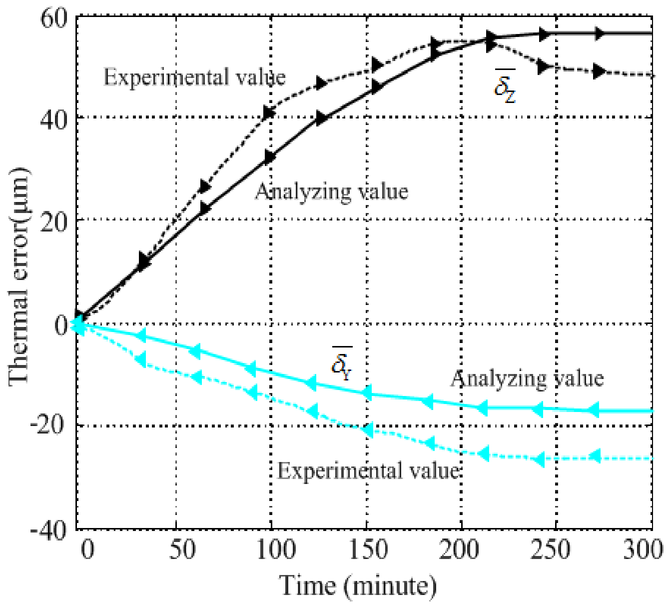

(a) Linear thermal errors

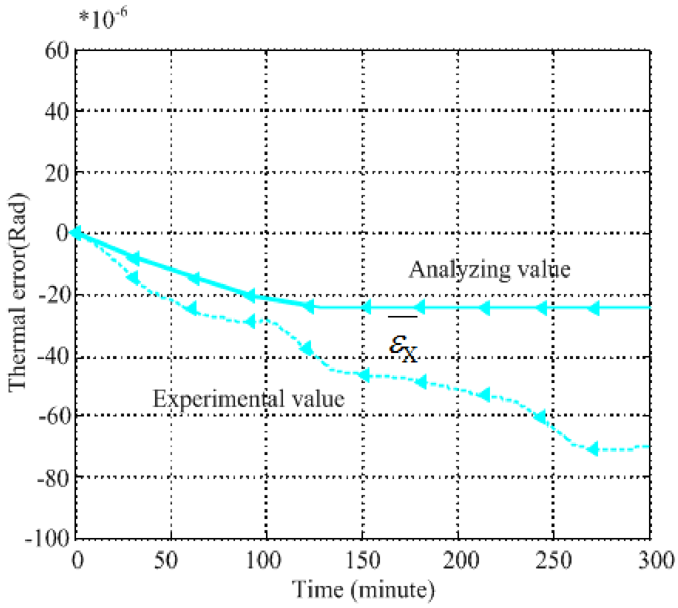

(b) Angular thermal error

Fig. 20. Spindle thermal error comparisons between experimental data and modeling results (T_S=20℃)